January 2015

Transient Response of a Liquid Injector to a Steep-Fronted Transverse Pressure Wave

Dasheng Lim
Purdue University

Graduate School Form 30
Updated 1/15/2015

PURDUE UNIVERSITY
GRADUATE SCHOOL
Thesis/Dissertation Acceptance

This is to certify that the thesis/dissertation prepared

By Dasheng Lim

Entitled

Transient Response of a Liquid Injector to a Steep-Fronted Transverse Pressure Wave

For the degree of Master of Science in Aeronautics and Astronautics

Is approved by the final examining committee:

Stephen D. Heister
Chair

Timothée L. Pourpoint

Carson D. Slabaugh

To the best of my knowledge and as understood by the student in the Thesis/Dissertation Agreement, Publication Delay, and Certification Disclaimer (Graduate School Form 32), this thesis/dissertation adheres to the provisions of Purdue University's "Policy of Integrity in Research" and the use of copyright material.

Approved by Major Professor(s): Stephen D. Heister

Approved by: Weinong Chen 11/19/2015

Head of the Departmental Graduate Program Date

TRANSIENT RESPONSE OF A LIQUID INJECTOR TO A STEEP-FRONTED TRANSVERSE PRESSURE WAVE

A Thesis

Submitted to the Faculty

of

Purdue University

by

Dasheng Lim

In Partial Fulfillment of the

Requirements for the Degree

of

Master of Science in Aeronautics and Astronautics

December 2015

Purdue University

West Lafayette, Indiana

For my parents

ACKNOWLEDGMENTS

I'd like to thank my advisor, Dr. Stephen D. Heister, for his patient guidance and sagely advice. My gratitude goes to my colleagues David Stechmann, Brandon Kan, Brent Justice, Swanand Sardeshmukh, and managing director Scott Meyer for all the help they've offered along the way, and also to Dr. Timothée Pourpoint's and Dr. William Anderson's groups for sharing their equipment and facilities for my experiments. Our machinist, Rob McGuire, deserves special credit for his excellent machining support, oftentimes on short notice. This study was made possible by the AFOSR.

TABLE OF CONTENTS

Page

LIST OF TABLES vi

LIST OF FIGURES vii

NOMENCLATURE xiii

ABSTRACT xiv

CHAPTER 1. INTRODUCTION 1

1.1 Overview 1

1.2 Motivation 2

1.3 Objectives 3

1.4 Past Works 4

1.5 Methodology 5

CHAPTER 2. FACILITIES AND HARDWARE 6

2.1 Laboratory Facilities 6

2.2 Test Setup 7

2.2.1 Pre-Detonator 7

2.2.2 Test Article 10

2.2.3 Water Feed System 11

2.2.4 Instrumentation 12

2.2.5 Test Stand 13

2.3 Test Sequence and Matrix 13

2.3.1 Injector Designs 14

2.3.2 Manifold Pressure Levels 16

CHAPTER 3. MODEL DEVELOPMENT 17

3.1 Fixed-Mass Model 17

Page

3.1.1 Response to a Step Change in Downstream Pressure 21
3.1.2 Response to a Sawtooth Profile in Downstream Pressure 23
3.1.2.1 Effect of Decay Time 24
3.1.2.2 Effect of Disturbance Amplitude under Constant Impulse Conditions .. 27
3.1.3 Timestep Sensitivity Study 30
3.2 Variable-Mass Model 34
CHAPTER 4. RESULTS AND ANALYSIS 36
4.1 Pressure Data 37
4.2 Qualitative Image Analysis 40
4.3 Quantitative Measurements from Video Data 44
4.4 Error in Backflow Distance 48
4.5 Error in Refill Time 50
4.6 Potential Contributions to Error 52
CHAPTER 5. CONCLUSIONS AND RECOMMENDATIONS 58
5.1 Conclusions 58
5.2 Recommendations for Future Work 59
LIST OF REFERENCES 61
APPENDICES
Appendix A Hardware Design and Technical Specifications 63
Appendix B Additional Results and Figures 66

LIST OF TABLES

Table Page

Table 2-1. Table of injector parameters for tested designs. 14

Appendix Table

Table B-1. Integrated pressure wave impulse size corresponding to each test run for Design L. 66

Table B-2. Integrated pressure wave impulse size corresponding to each test run for Design M. 67

Table B-3. Integrated pressure wave impulse size corresponding to each test run for Design S. 68

Table B-4. Integrated pressure wave impulse size corresponding to each test run for Design P. 69

LIST OF FIGURES

Figure Page

Figure 2-1. P&ID of the DVRC igniter panel feed system. 7

Figure 2-2. Predet used to initiate detonation wave upstream of the test article. 8

Figure 2-3. P&ID of predet system. 9

Figure 2-4. Schlieren image of predet firing test showing emergence of detonation wave from DDT tube. Recorded at 512 by 128 pixels resolution and 29,197fps. Images courtesy of Brandon Kan and Brent Justice. 10

Figure 2-5. Drawing of acrylic test article. 11

Figure 2-6. Test stand comprising test article, predet, buffer tank, needle valve, and pressure transducers. 13

Figure 2-7. Drawings of tested injector designs. From left to right: L, M, S, and P. 14

Figure 2-8. Plot of discharge coefficients of injectors used in experiments 16

Figure 3-1. Schematic of sequence of events for a fixed mass subjected to change in pressure differential. 18

Figure 3-2. Plot of non-dimensional response time vs. non-dimensional manifold pressure ratio. 21

Figure 3-3. Plot of non-dimensional backflow time and non-dimensional response time vs. non-dimensional manifold pressure ratio. 23

Figure Page

Figure 3-4. Plot of pressure profiles with constant peak pressure and varying decay times. 25

Figure 3-5. Plot of non-dimensional velocity vs. non-dimensional time for various decay times. P_m/P_2=0.1. 25

Figure 3-6. Plot of non-dimensional displacement vs. non-dimensional time for various decay times. P_m/P_2=0.1. 26

Figure 3-7. Plot of non-dimensional recovery time vs. non-dimensional decay time. P_m/P_2=0.1. 26

Figure 3-8. Plot of pressure profiles with constant total impulse. 28

Figure 3-9. Plot of non-dimensional velocity vs. non-dimensional time for various decay times and peak pressures. 28

Figure 3-10. Plot of non-dimensional displacement vs. non-dimensional time for various decay times and peak pressures. 29

Figure 3-11. Plot of non-dimensional recovery time vs. non-dimensional decay time. ... 29

Figure 3-12. Plot of interface velocity vs. time showing solution convergence at timestep Δt=1e-8s for τ_c/τ=0.25. 31

Figure 3-13. Plot of interface location vs. time showing solution convergence at timestep Δt=1e-8s for τ_c/τ=0.25. 31

Figure 3-14. Plot of interface velocity vs. time showing solution convergence at timestep Δt=1e-8s for τ_c/τ=1.00. 32

Figure 3-15. Plot of interface location vs. time showing solution convergence at timestep Δt=1e-8s for τ_c/τ=1.00. 32

Figure Page

Figure 3-16. Plot of interface velocity vs. time showing solution convergence at timestep Δt=1e-8s for τ_c/τ=0.25. 33

Figure 3-17. Plot of interface location vs. time showing solution convergence at timestep Δt=1e-8s for τ_c/τ=0.25. 33

Figure 4-1. Macroscopic view of events during a typical test run. Pressure wave travels from top to bottom and liquid flow is from left to right. Recorded at 12,012fps and 304 by 512 pixels resolution. 36

Figure 4-2. Typical pressure trace recorded during tests using designs M, S and P. Red line represents atmospheric pressure of 14.7 psia. 38

Figure 4-3. Typical pressure trace recorded during tests using design L. Red line represents atmospheric pressure of 14.7 psia. 38

Figure 4-4. Pressure trace supporting explanation of large-amplitude pressure excursion resulting from thermal drift. 39

Figure 4-5. Overlay of 23 pressure traces with minimal thermal drift showing consistency of measurements. 39

Figure 4-6. Representative pressure trace used as input for numerical model. Thermal drift is still visible here but is of small amplitude and short duration. 40

Figure 4-7. Sequence of images from left to right showing combustion gas penetrating into injector plenum. Detonation wave travels from left to right and liquid flows from bottom to top. Recorded at 88,888fps and 208 by 56 pixels resolution. 41

Figure Page

Figure 4-8. Sequence of images from left to right showing partial injector backflow. Detonation wave travels from left to right and liquid flows from bottom to top. Recorded at 83,33fps and 240 by 56 pixels resolution. 41

Figure 4-9. Sequence of images from left to right showing limited backflow at high injector pressure gradient. Detonation wave travels from left to right and liquid flows from bottom to top. Recorded at 88,888fps and 208 by 56 pixels resolution. 42

Figure 4-10. Plot of non-dimensional backflow distance vs. non-dimensional pressure drop across injector. 44

Figure 4-11. Plot of non-dimensional refill time vs. non-dimensional pressure drop across injector. 45

Figure 4-12. Sample output plots obtained from variable-mass model. Upper left: input pressure signal. Lower left: net acceleration on liquid column. Upper right: velocity of liquid-gas interface. Lower right: location of liquid-gas interface. 46

Figure 4-13. Plot of absolute error in backflow distance vs. non-dimensional pressure drop. 49

Figure 4-14. Plot of non-dimensional error in backflow distance vs. non-dimensional pressure drop. 49

Figure 4-15. Plot of non-dimensional error in backflow distance vs. Reynolds number. 50

Figure 4-16. Plot of absolute error in refill time vs. non-dimensional pressure drop. 51

Figure 4-17. Plot of non-dimensional error in refill time vs. non-dimensional pressure drop. 51

Figure 4-18. Plot of non-dimensional error in refill time vs. Reynolds number. 52

Figure Page

Figure 4-19. Axial velocity profile at exit of injector design L at ΔP = 5psi. 53

Figure 4-20. Plot of non-dimensional boundary layer thickness vs. Reynolds number showing power curve fits. 54

Figure 4-21. Plot of non-dimensional error in backflow distance vs. non-dimensional boundary layer thickness..... 55

Figure 4-22. Plot of non-dimensional error in refill time vs. non-dimensional boundary layer thickness. 55

Figure 4-23. Discharge coefficient vs. pressure drop of tested injectors..... 57

Appendix Figure

Figure A-1. Drawing of transition channel section showing major dimensions in inches. 63

Figure A-2. Drawings of injector modules showing major dimensions in inches. All injector orifices have a diameter of 0.033in (0.84mm). 64

Figure A-3. Technical specifications of Kulite™ XTEL-190 high frequency pressure transducer used in pressure wave measurement. Extracted from http://www.kulite.com. 65

Figure B-1. Snapshots of instances at which maximum backflow is attained for each test using 0.30in injector. Manifold pressure in (a): 15.7psia, (b): 16.8psia, (c): 17.8psia. 70

Figure B-2. Snapshots of instances at which maximum backflow is attained for each test using 0.30in injector. Manifold pressure in (d): 18.7psia, (e): 19.7psia. 70

Figure B-3. Snapshots of instances at which maximum backflow is attained for each test using 0.20in injector. Manifold pressure in (a): 15.6psia, (b): 16.7psia, (c): 17.7psia. Higher manifold pressures not shown due to similarity of backflow extent as (c)..... 71

Figure Page

Figure B-4. Snapshots of instances at which maximum backflow is attained for each test using 0.15in injector. Manifold pressure in (a): 15.6psia, (b): 16.9psia, (c): 17.8psia. 71

Figure B-5. Snapshots of instances at which maximum backflow is attained for each test using 0.15in injector. Manifold pressure in (d): 18.5psia, (e): 19.7psia. 72

Figure B-6. Snapshots of instances at which maximum backflow is attained for each test using 0.15in injector with reduced plenum. Manifold pressure in (a): 15.6psia, (b): 16.7psia, (c): 17.5psia. Higher manifold pressures not shown due to similarity of backflow extent as (c). 72

NOMENCLATURE

a	=	acceleration [m/s^2]
A	=	area [m^2]
D	=	orifice diameter [m]
f	=	Fanning friction factor [ ]
F	=	force [N]
L	=	injector length [m]
m	=	mass of liquid [kg]
P	=	pressure [Pa]
p	=	pressure ratio P_m/P_2
v	=	interface velocity [m/s]
x	=	interface location [m]
S	=	shear stress [Pa]
t	=	time [s]
ε	=	surface roughness [m]
μ	=	dynamic viscosity [Pa.s]
ρ	=	density [kg/m^3]
τ	=	time constant [s]

Subscripts

1	=	before step change
2	=	after step change
avg	=	weighted average
b	=	backflow
c	=	pressure decay time
e	=	orifice exit
fric	=	friction
m	=	manifold
o	=	orifice
pg	=	pressure gradient
r	=	response time
wet	=	wetted surface

ABSTRACT

Lim, Dasheng. M.S.A.A., Purdue University, December 2015. Transient Response of a Liquid Injector to a Steep-Fronted Transverse Pressure Wave. Major Professor: Stephen D. Heister.

A series of experiments has been performed at ambient pressure using optically accessible test articles to study the dynamic response of a liquid injector subjected to a steep-fronted transverse pressure wave. The pressure differential across the injectors was varied between 1 and 5 psig. High speed video images revealed the highly complex and multi-dimensional nature of the flow response. Results also suggest that the diameter of the plenum immediately upstream of the injector influences dynamic response; a narrower plenum dampens it. A one-dimensional, lumped parameter model was also developed to predict injector response. Results were compared with empirical data, and the model was found to show promise in predicting backflow distance at the high end of tested pressure differentials. Its ability to predict injector recovery time remains inconclusive. The cause of deviation in the model's predictions is believed to be the boundary layer effects along the injector channel wall. Further studies at elevated pressures will provide useful insights for improving the model.

CHAPTER 1. INTRODUCTION

1.1 Overview

Pressure gain combustion (PGC) research has been rapidly gaining attention as a potential means to produce thrust or generate power at higher efficiency than conventional technology[1,2]. PGCs are transient devices which rely on the detonative mode of combustion as opposed to deflagration at constant pressure, as is common in modern rocket or air-breathing engines. The most commonly known and better understood PGC is the pulse detonation engine (PDE) and recently, the rotating detonation engine (RDE) has become increasingly popular as a candidate for future applications. The primary difference between them is the direction of detonation wave travel. In a PDE, detonation waves propagate axially along the combustion chamber; in a RDE, the combustion chamber takes the form of an annulus and detonation waves move azimuthally around it.

In a typical PDE, propellant flow is controlled using high-speed valves. Each operating cycle involves propellant fill, ignition, deflagration-to-detonation transition (DDT), and blowdown. Due to the fact that a PDE requires time to fill and blowdown, its operating frequency is often limited to only a few hundred hertz[3]. Since thrust is produced by each pulse, it follows that a higher operating frequency is desirable. The requirement for DDT also leads to a long combustion chamber which adds to its weight penalty. Lastly, the need for valve and ignition controls drastically increases the complexity of the system.

Herein lies the advantage of a RDE. It does not rely on valves and ignition is required only once at the beginning of operation. Without the need for valve and ignition

control, the system is greatly simplified. Since propellants are fed constantly and detonation is only established once, a RDE can operate at frequencies of the order of several kilohertz[4].

While the RDE possesses advantages over the PDE, it comes with its own caveats. Even though propellant flow is globally constant, it varies locally. During ideal operation, the high pressure region behind detonation wave causes propellant flow to cease momentarily. This prevents flameholding which could force the device into a constant pressure mode of operation and is therefore a critical feature of a RDE injector. The propellant flow must then recover to allow the perpetuation of the detonation wave as it comes back around the annulus. Prior studies by Bykovskii[5] have shown the critical fill height, which is the layer thickness of fresh propellants needed to sustain stable detonation, to be between seven and 12 times the detonation cell width which depends on the propellant combination and initial pressure. Since this all has to happen several thousand times every second, it becomes immediately clear that the injector operates under highly transient conditions. It is for this reason that the injector's transient response becomes extremely important.

Depending on the strength of the detonation wave and pressure gradient across the orifice, propellant mass flow could either decrease or cease completely. In the latter case, propellant flows in a reverse direction back towards the manifold and the injector orifice could be completely vacated. It is postulated at this time that it may be desirable to have the propellant flow cease momentarily to prevent flameholding. Following injector check-off, flow has to recover and be able to refill the chamber with fresh propellants to the critical fill height before the next detonation wave arrives.

1.2 Motivation

From the principles of RDE operation outlined above, it is clear that possessing knowledge of the transient response of an injector is a critical step in building a working engine. Compounded by the recent commencement of RDE research at Purdue University,

the motivation naturally exists for this study to gain understanding of the transient behavior of a liquid injector as a detonation wave interacts with the injector orifice. Unfortunately, there exists a dearth of literature in this subject as nearly all current devices operate in quasi-steady fashion. The combustion efficiency of any type of combustor is strongly influenced by its injector. Therefore, injector design forms a large part of the effort in building an engine. This is even more so for a RDE; while a constant pressure engine would merely operate at a lower efficiency with a poorly designed injector, a RDE may not even operate in detonative mode. Given the high cost of hardware development, trial and error is not an option. It is essential that we develop the capability to predict and control injector response to improve chances of successful engine design. Additionally, having this capability will also provide insight on the data collected from RDE test fires as well as guide future design iterations.

While commercial computational fluid dynamics (CFD) programs are available for simulating multiphase flows, such analyses are time consuming because of meshing requirements. If a simple 1-D force-balance model could be used to predict a plain orifice injector's dynamic response to acceptable accuracy, it would be an extremely useful tool for generating preliminary designs. Without the need to create meshes, time can be saved especially when many different injector configurations are to be considered.

1.3 Objectives

The goal of this study is to investigate the response of a liquid injector at the microsecond timescale and develop a 1-D numerical model for a plain orifice injector which is able to predict the backflow and recovery of a liquid injector when a pressure signal is applied to its outlet. The model will be compared with high speed videos and pressure data gathered from experiments for validation. If successful, the model will be used as a preliminary design tool for future RDE injectors using liquid propellants. Ultimately, the goal is to achieve the capability to quantify an injector's behavior to complement the RDE research efforts at Purdue University.

1.4 Past Works

At the time of writing, there had been no published empirical study of injector response of similar type. In her 2006 M.S. thesis, Megan MacDonald[6] investigated the nonlinear dynamic response of an injector. The research was motivated by prior studies on combustion instability and was primarily concerned with the frequency response of a plain orifice injector when subjected to sinusoidal perturbances in chamber pressure. It cites NASA SP-194[7] and Reba and Brosilow[8] for the modeling of a fluid system as an analog of a RLC circuit. While the pressure signals relevant to MacDonald's study differ from those seen in RDEs, the fluid system models used are pertinent to the current study and serve to confirm the suitability of the models used here.

Motivated by the hydrodynamics of solid spheres suspended in fluids, Felderhof conducted a numerical study[9] where a sudden impulse was introduced at a point along the longitudinal axis of a circular tube by means of suddenly setting a small sphere in motion. It was mentioned in the report that wall interaction is an important factor in a confined flow because the flow acts back on any particle moving within it. The study was focused on the fundamental flow features such as eddy formation and velocity components, and as such was of limited utility to the RDE research conducted at Purdue.

Braun et al.[10], similarly motivated by RDE injection systems, published a paper on an experimental study on the response of gaseous fluidic valves in 2011. In their study, pressure transducers mounted within the injector plenum were used to infer the shock front location and duration for which injection was interrupted. It was found that the interruption time divided by the characteristic time constant of the detonation vessel follows a linear trend with a non-dimensional pressure ratio between the plenum and C-J detonation pressure. Additionally, the type of fuel appeared to be of minor influence to the trend. However, they were unable to track the interface between detonation products and fresh propellants due to the lack of optical access in their hardware. Because of this, they could not ascertain the time it took for fresh propellant mixture to be injected

following the detonation wave. The use of gaseous propellants also meant that the flow dynamics are significantly different from that of a liquid.

More recently, Naples et al. performed a series of experiments[11] where a hot-film anemometer was used to measure flow velocity in the fuel plenum of a RDE. They found that flow velocity in the fuel plenum fluctuated significantly, but not necessarily at the same frequency as the detonation wave passage in the combustion chamber. While their experiment highlighted the highly transient nature of the injector, the use of gaseous propellants makes their injector much more agile than their liquid counterparts in terms of flow disturbance. Compressibility of the fluid also causes its flow characteristics to differ from that of liquid propellants.

1.5 Methodology

To meet the objectives of the study, a sub-scale experiment was designed to represent a single injector element of a RDE. A “pre-detonator” was used to drive a detonation through an optically-accessible test section and a high speed camera recorded the response of the liquid – water in this case – as the detonation wave passes. A high speed pressure transducer was used to record the pressure trace of the detonation wave, which would be used as the input for the numerical model which will be described in Chapter 3.

From the high speed camera footage, the backflow distance and refill time of the various injectors were measured. The data were then compared with the numerical model. While the mode of operation of a RDE is significantly different from that of the experiment, it should be theoretically possible to extend the same treatment to any input pressure signal to obtain the corresponding transient response prediction of the injector. Results of the experiments are presented in Chapter 4.

CHAPTER 2. FACILITIES AND HARDWARE

2.1 Laboratory Facilities

The experiments were performed at the High Pressure Lab (HPL), which provides high pressure hydrogen, oxygen, and nitrogen in both bulk and bottled forms. For this series of experiments, gaseous hydrogen and oxygen were fed from 5000psi K-bottles while nitrogen was tapped from HPL's bulk nitrogen supply. A deionized water supply system provides students with high-purity water used in rigorous hardware cleaning procedures as well as for testing purposes. The lab is also furnished with both high and low speed data acquisition (DAQ) systems to cater to different experimental requirements. The high speed DAQ is capable of sampling each channel at up to 1MHz and the low speed DAQ acquires at rates up to 5kHz.

An existing igniter panel built for another experiment by B.J. Austin of IN Space LLC and Dr. William Anderson's group served as the propellant feed system for the hydrogen/oxygen pre-detonator (henceforth referred to as "predet"). It consists of hydrogen, oxygen, and nitrogen lines each comprising a manual isolation valve leading to a manual pressure regulator which sets the corresponding pressure levels for the feed system. The lines are then followed by pneumatically-actuated run valves and check valves before feeding into the predet system. A plumbing and instrumentation diagram of the feed system is shown in Figure 2-1.

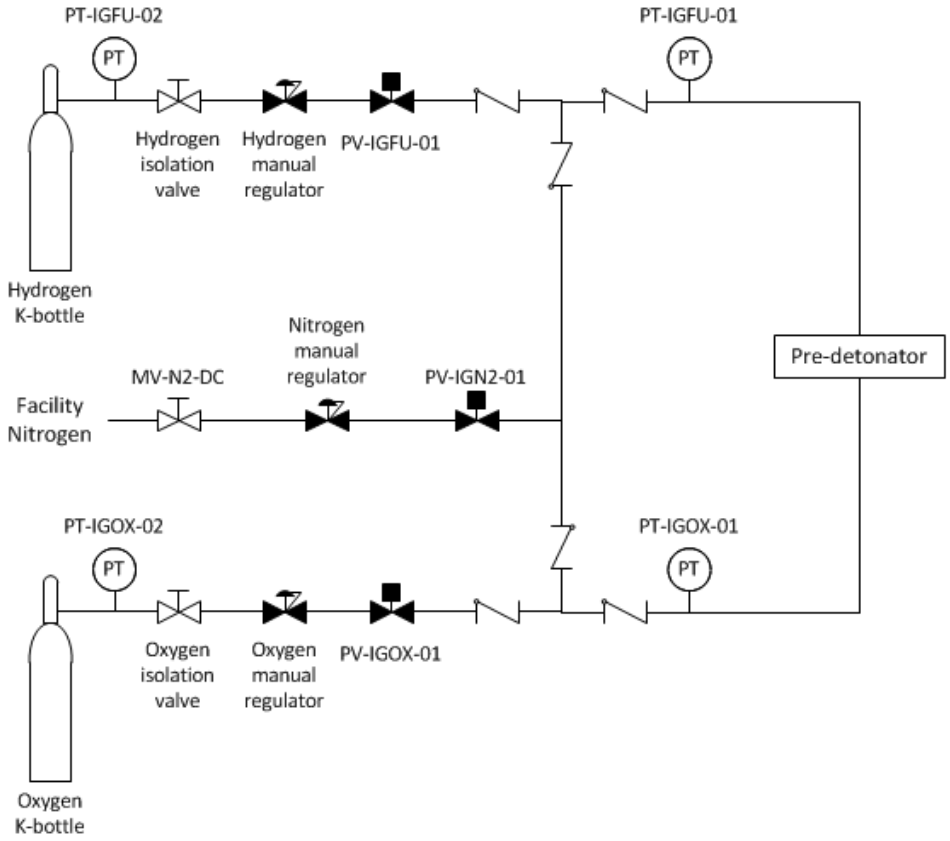

Figure 2-1. P&ID of the DVRC igniter panel feed system.

2.2 Test Setup

2.2.1 Pre-Detonator

The design of the predet was provided by Dr Frederick Schauer's group at AFRL and built by Brandon Kan[1] at Zucrow Labs. Figure 2-2 shows a picture of the predet with labels to its major components. It is a deflagration-to-detonation transition (DDT) device which depends on combusting the mixture in a long tube containing a spiral obstruction to achieve DDT. The primary components of the device are listed as follows:

- 2x Swagelok™ 2μm particulate filters
- 2x The Lee Company™ solenoid valves

[1] Ph.D. student, Purdue University School of Aeronautical and Astronautical Engineering

    - P/N: IEPA2411141H (oxygen)
    - P/N: IEPA2411241H (hydrogen)
- 1x Swagelok™ 1/16in cross
- 1x 1/4in tube approximately 4in long, tapped
- 1x NGK™ spark plug
    - Model: ME-8

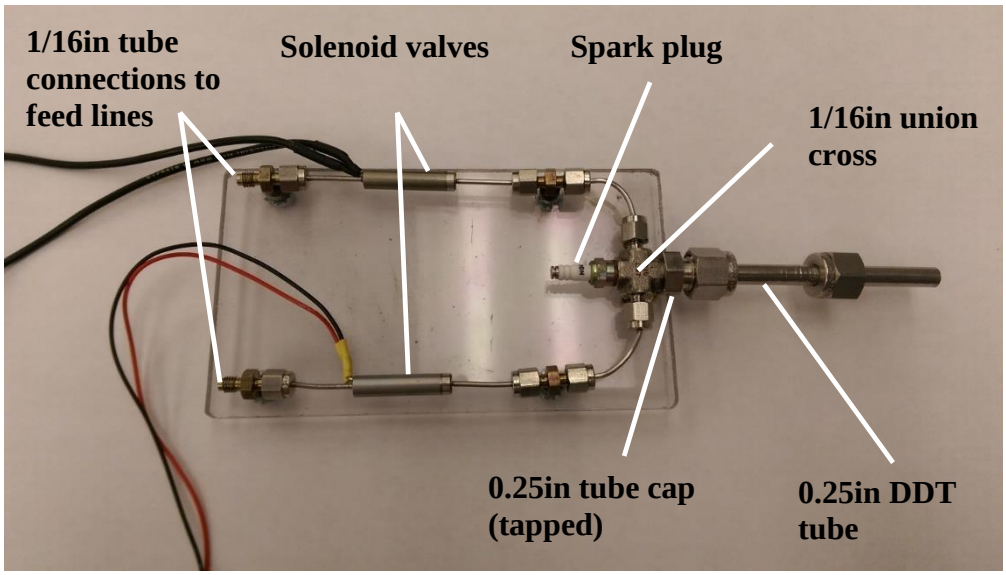

Figure 2-2. Predet used to initiate detonation wave upstream of the test article.

To accommodate the spark plug, the male threads on one side of the 1/16in union cross was machined off and a ¼-32 thread was tapped. On the opposite end, a 0.25in tube cap was bored through and tapped with a 10-32 thread into which the union cross was fastened. The 0.25in tube cap formed the connection from the cross to the DDT tube. The DDT tube was a 0.25in stainless steel tubing threaded on the upstream end to emulate a Shchelkin spiral which is commonly used to promote DDT. The components were mounted on a piece of acrylic sheet for structural support and connected using 1/16in stainless steel tubes and Swagelok™ compression fittings. 1/16in tubes fed hydrogen and oxygen from the igniter panel to the connection locations indicated in Figure 2-2. Prior to entering the 1/16in feed lines, the hydrogen and oxygen are passed through 2µm particulate filters to ensure that the lines do not get clogged by any debris which might be present. Injection into the union cross is controlled using the fast-response solenoid

valves. The union cross serves as the main chamber of the predet. Here the propellants are mixed and ignited with a spark discharge. An auto-sequence controller was developed by Brandon Kan and Brent Justice[2] for the purpose of timing the solenoid valves and spark plug for firing. After ignition, the hot gas expands through the DDT tube before entering the test article. A P&ID of the predet system is shown in Figure 2-3.

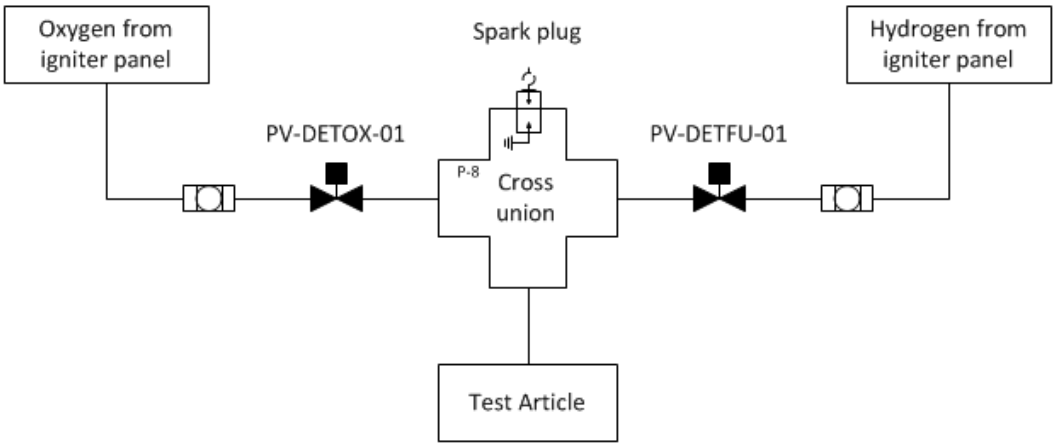

Figure 2-3. P&ID of predet system.

To verify that the predet functions as intended, a firing test was conducted and supplemented with Schlieren imaging using a high speed camera. Figure 2-4 shows the density gradient associated with a shock wave exiting from the DDT tube followed closely by what is presumed to be combustion products, indicating that a detonation wave has been successfully produced.

[2] Former Undergraduate student, Purdue University School of Aeronautical and Astronautical Engineering

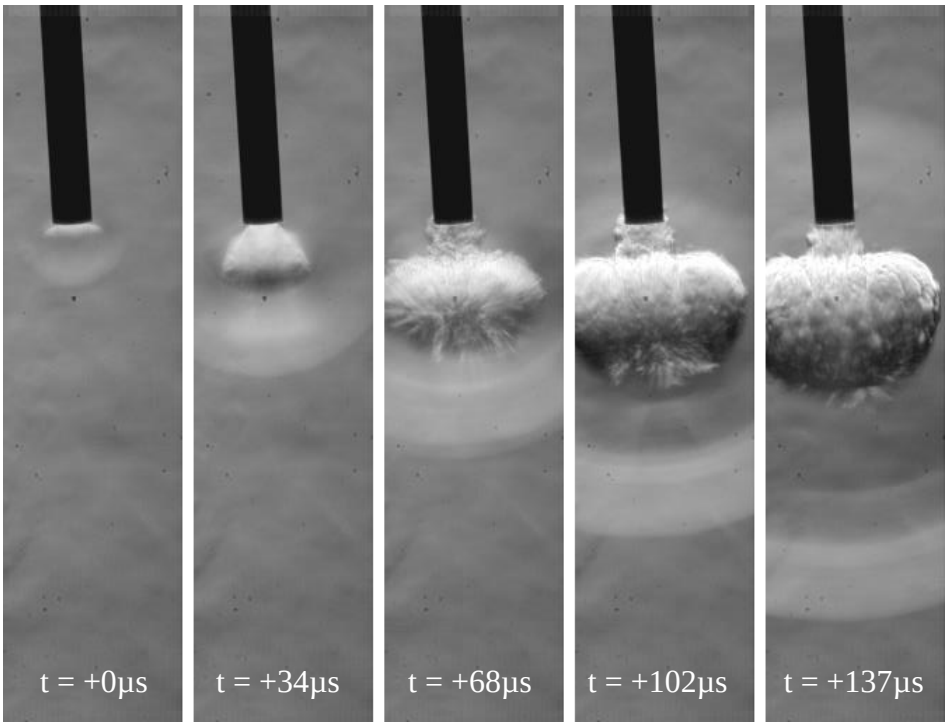

Figure 2-4. Schlieren image of predet firing test showing emergence of detonation wave from DDT tube. Recorded at 512 by 128 pixels resolution and 29,197fps. Images courtesy of Brandon Kan and Brent Justice.

2.2.2 Test Article

Test articles (driven section) were fabricated from clear acrylic to provide optical access to the injector. A test article comprises two main parts: a transition channel section and an injector module. Each part in turn consists of a main channel/injector geometry and a clear cover piece which closed off the detonation channel. All components of the test article were held together using an acrylic cement. Drawings of the components with major dimensions can be found in the Appendix. The transition channel section was reused while the injector modules were cut off and replaced with the various designs for different tests. This allowed hardware fabrication cost to be kept at a minimum. At the head end of the test article is a 0.25in compression tube fitting through which the predet's driver tube connects to the driven section. Immediately downstream is a diffuser section which helps to keep the detonation wave attached to the channel walls as it transitions

from a circular tube into a rectangular channel of larger area. Following the diffuser section is a straight channel along which the liquid injector is situated. Channel width was chosen to be 0.18in to match the inner diameter of the 0.25in DDT tube, and its height was made three times of its width (0.54in) such that a flat rectangular profile was obtained. A high frequency pressure transducer is located at the same axial station under the assumption that pressure will be uniform across the channel cross section. A drawing of the test article is shown in Figure 2-5.

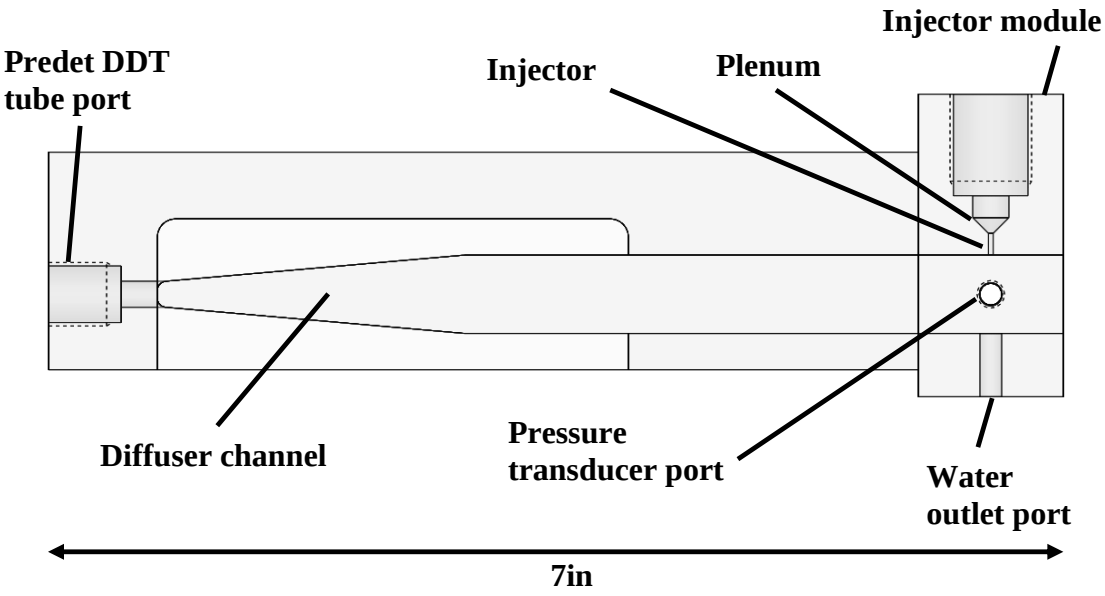

Figure 2-5. Drawing of acrylic test article.

2.2.3 Water Feed System

The test article's injector was originally connected directly to the facility's deionized water supply line. However, initial runs of the experiment revealed large pressure fluctuations in the line and a 1-liter tank was subsequently installed to serve as a pressure disturbance dampener. A needle valve downstream of the tank was used to control the manifold pressure of the injector which was measured approximately 3in upstream of the injector.

2.2.4 Instrumentation

A list of the instrumentation and equipment used for the experiments is shown here:

- 1x GE Druck™ 60psia pressure transducer
- 1x Kulite™ XTEL-190 1000psia high frequency pressure transducer
- Vision Research Phantom™ v7.1 high speed camera
- Infinity™ K2/SC long distance microscope lens
- 1x 500W halogen lamp

The 60psia pressure transducer was used to provide manifold pressure readings. However, since real-time manifold pressure was not required in the study, it was not recorded. The critical pressure measurement was that of the transverse pressure wave, measured with the high frequency 1000psia transducer. Data from this transducer was sampled at 1MHz in order to capture the peak amplitude of the detonation wave. The signal was also passed through a signal conditioner with an amplification factor of 50 because of the low relative signal output generated by the pressure wave at ambient test conditions.

2.2.5 Test Stand

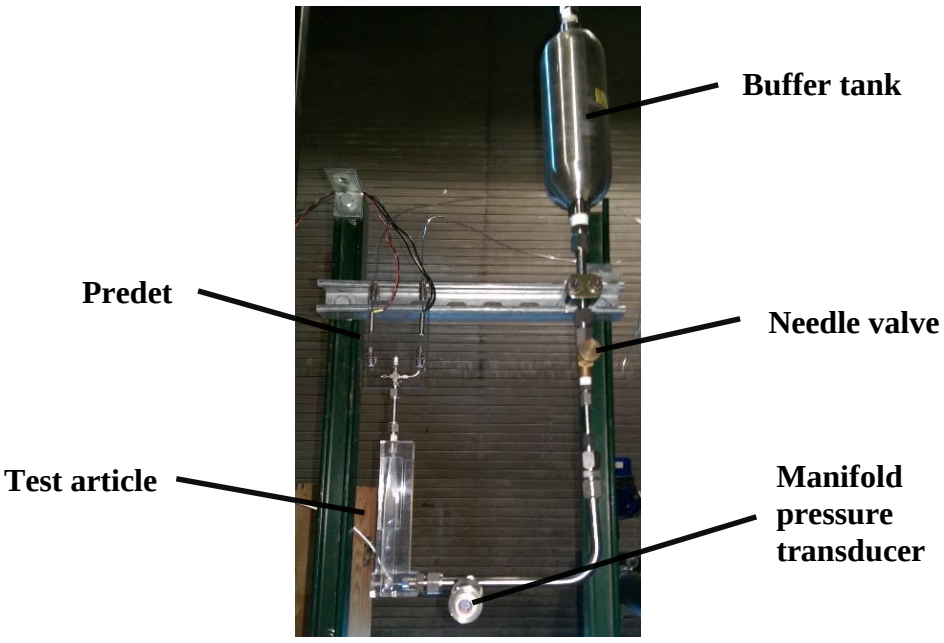

Figure 2-6. Test stand comprising test article, predet, buffer tank, needle valve, and pressure transducers.

The hardware for the experiment were fastened to a frame constructed using unistruts and the complete test stand is shown in Figure 2-6. The test article was placed between a light source and the high speed camera (not shown in picture). A long-distance microscope lens attached to the high speed camera provided a magnified view of the injector. To minimize image smearing at high frame rates, a short exposure time was necessary. This in turn required the test section to be brightly lit. A 500W halogen lamp provided the strong backlight required to illuminate the test section.

2.3 Test Sequence and Matrix

In a typical test, the solenoid valves were opened for 1.5s to overfill the predet and test article with hydrogen/oxygen mixture and closed to prevent backflow of detonation products into the feed system. The feed pressure for both hydrogen and oxygen was set at 200psia. Assuming that the lines were choked, the equivalence ratio of

the mixture was approximately 2 so a deviation from C-J detonation was expected. At the same time the valves closed, the high speed camera was triggered to commence image recording. 3ms after the valves were closed, the spark plug discharged for approximately 3ms, igniting the mixture. The DDT process occurred within the predet tube and the resulting detonation wave propagated through the test article, driving the response of the injector.

Four different injector configurations were designed and produced for the experiments. For simplicity, the configurations will be designated L (long), M (medium), S (short), and P (plenum) to represent their respective major design features.

2.3.1 Injector Designs

Table 2-1. Table of injector parameters for tested designs.

Design	**Orifice diameter D [in]**	**Injector length L [in]**	**Plenum diameter [in]**
L (Long)	0.033	0.30	0.25
M (Medium)	0.033	0.20	0.25
S (Short)	0.033	0.15	0.25
P (Plenum)	0.033	0.15	0.081

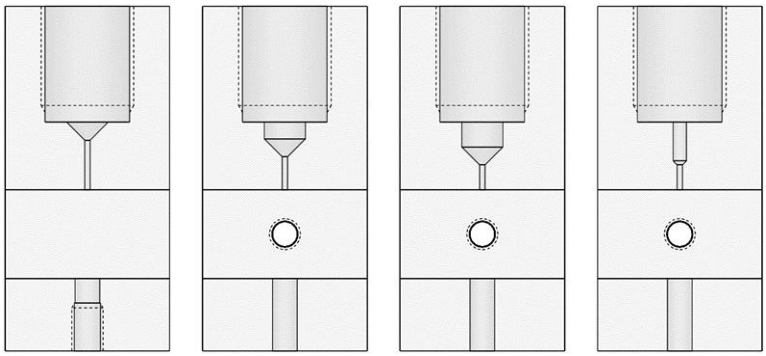

Figure 2-7. Drawings of tested injector designs. From left to right: L, M, S, and P.

The injector is a plain orifice 0.033in in diameter for all four configurations. The diameter was originally based on a scaled multiple of that in the RDE prototype which was concurrently being developed, but later increased to 0.033in for manufacturing purposes. In the first three configurations, the different orifice lengths tested were 0.30in, 0.20in and 0.15in. Upstream of the orifice is a 0.25in plenum to minimize dynamic pressure. The fourth configuration is an injector with a 0.15in long orifice, but with a 0.081in plenum instead. The purpose of the fourth configuration is to study the effects of injector plenum cross section on the injector's flow resistance. Dynamic pressure in the plenum was kept under 0.7% of manifold pressure for Design P, which had the greatest dynamic pressure in that region. Water flow tests were conducted using the catch and weigh method to determine the discharge coefficient C_d of the orifices and the results are plotted in Figure 2-8.

The water flow test was performed over a range of low pressure drops using the facility's deionized water system. From the chart, it is immediately clear that at these low pressure drops, the boundary layers in the injectors are still developing and their discharge coefficients are therefore not constant. At yet lower pressure drops such as those corresponding to the injector response experiments, discharge coefficients are expected to be even lower and more sensitive to changes in pressure differential, i.e. the slope of the C_d vs. ΔP curves should be steeper. It is impractical in our case to perform experiments at pressure differentials which would result in steady C_d because the injectors are expected to be too stiff to show any significant response from the pressure wave.

After the initial test with the first injector configuration (L = 0.30in), it was discovered that the jet of water emerging from the injector was accumulating along the channel wall. The accumulation was sufficient to obstruct the flow path and cause inconsistent injector behavior under the same test conditions. Measurements from the pressure transducer were also affected in an unknown manner due to the interaction between the pressure wave and water layer. Subsequently, the test articles were modified such that a through hole was positioned directly across the injector to allow the water to

exit the detonation channel. The pressure transducer was relocated from the opposite wall to that adjacent to the injector. The change in design is shown in Figure 2-7 above. The corresponding data showed that the addition of the exit port was successful in eliminating the problem and led to consistent pressure readings and repeatable tests.

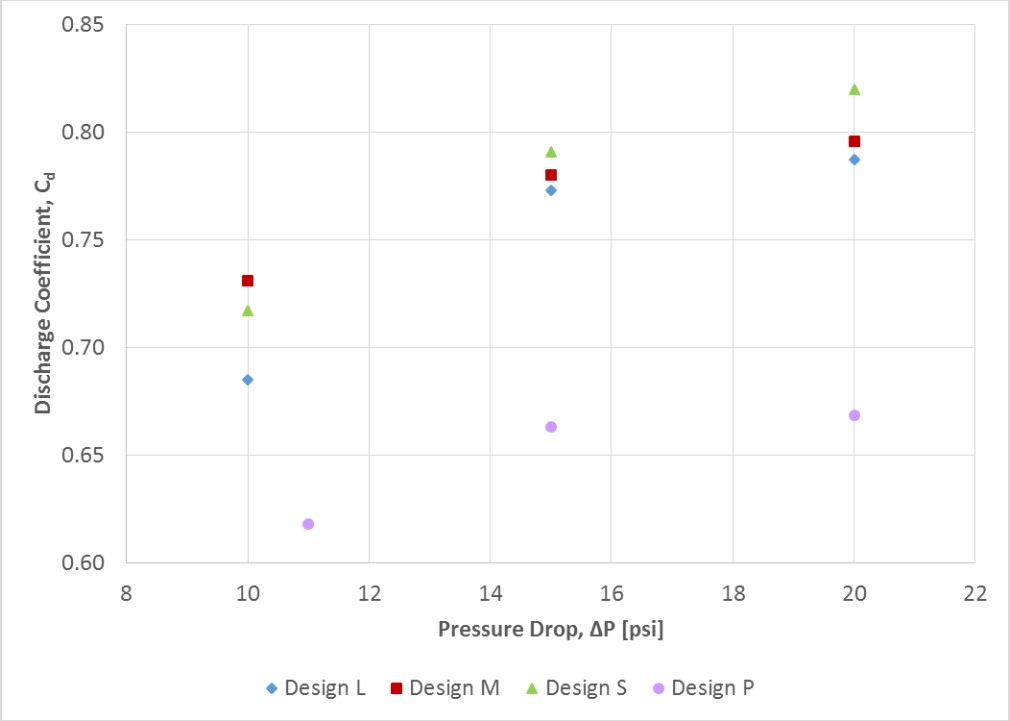

Figure 2-8. Plot of discharge coefficients of injectors used in experiments

2.3.2 Manifold Pressure Levels

Manifold pressure was measured along a section of 0.5in tubing approximately 3in upstream of the orifice. Five different manifold pressures were tested across all injector designs, ranging from approximately 15.7psia to 19.7psia in 1psia increments. Due to the random pressure fluctuations in the deionized water supply line, deviations of approximately ±0.2psi from set pressure were observed. Since the pressure differential across the orifice was only up to 5psi, the fluctuations resulted in significant uncertainty. However, it shall be seen in the next chapter that the data still show acceptable scatter.

CHAPTER 3. MODEL DEVELOPMENT

It is useful to consider the slug of fluid in the injector passage as a solid body in order to assess its dynamic response to the passage of a highly transient pressure wave. Here, the presumption is that the sound speed in the fluid is high such that the pressure difference between inlet plenum and chamber is immediately communicated to the entire column of fluid. The other assumption that is required for this simple model is that the mass of the column is fixed, i.e. fluid backflowing into the inlet manifold still participates in the overall dynamic response. This assumption is similar to virtual mass arguments that are employed in other contexts; i.e. there is some of the backflow momentum communicated to adjacent fluid in the manifold due to hydrodynamic and viscous interactions. The advantage of this simplification is that simple expressions can be derived for step changes or triangular pressure pulses and can provide insight into the dynamic response of the column in terms of backflow distance and response time. Section 3.1 of this chapter provides a description of the simple model and some parametric results.

In Section 3.2 we relax the assumption of fixed column length/mass which results in a second order system that must be integrated numerically. Here we also include viscous forces in order to assess their overall importance in these developing flows.

3.1 Fixed-Mass Model

A one-dimensional, lumped parameter computational model was developed to aid in injector design by solving for the dynamic response of a column of liquid with density ρ and length L to transient events in the combustion chamber as highlighted in Figure 3-1. We consider a fixed manifold pressure, P_m, and an initial chamber pressure of P_1. Also,

we define x as the location of the end of the column for the purposes of tracking its motion along the orifice passage.

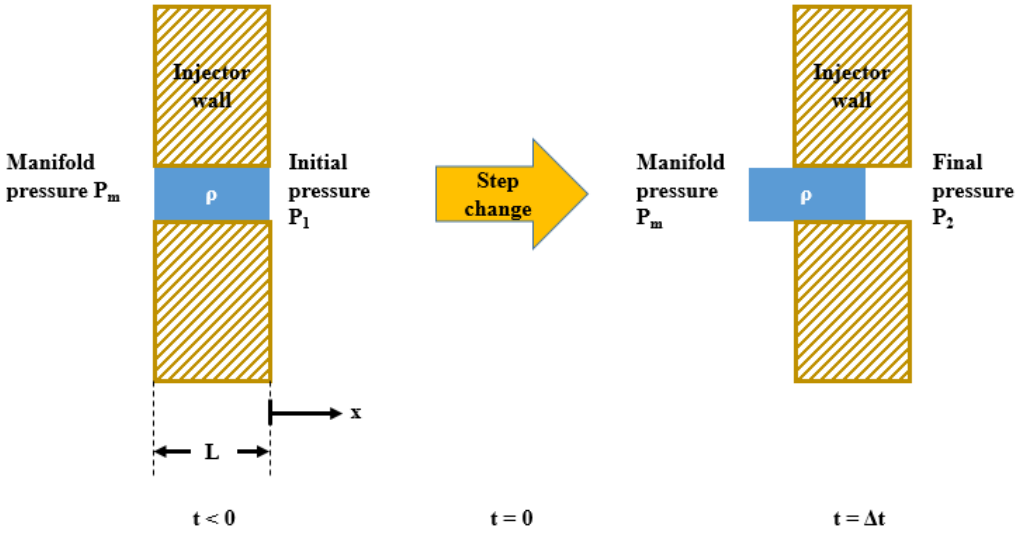

Figure 3-1. Schematic of sequence of events for a fixed mass subjected to change in pressure differential.

While injector flow dynamics have been of interest to the combustion stability and water hammer communities for many years, we have not found an analysis comparable to this simple approach in existing literature. By and large, the combustion stability community has assessed transient response to sinusoidal waveforms using both linear[7,8] and non-linear[6] models. In the water hammer application, finite wave speeds are considered as the applications typically stem from "long pipes" and linear and non-linear wave equations are employed to assess dynamics[12].

It is instructive to consider the response of this liquid column to a step change in chamber pressure from a level P_1 when $t < 0$ to a level P_2 for $t > 0$. The downstream pressure P_1 can be set to zero without loss of generality, i.e. we measure all pressure differences with respect to this initial gauge pressure.

Applying Newton's Second Law $\Sigma F = ma$ to the liquid column with $F = PA$ gives:

$$\rho L A_o \frac{dv}{dt} = A_o P_m - A_o P_e \pm \frac{1}{2}\rho v^2 \tag{3.1}$$

The dynamic pressure term appearing in equation (3.1) stems from the fact that the entire column is moving prior to a disturbance in the downstream pressure. Basically the entire manifold stagnation pressure has to be applied in order to stagnate the fluid. The upper sign applies when the flow is moving to the right (positive x direction) and the lower sign applies during backflow conditions. It becomes apparent from the above equation that for a plain orifice, the cross sectional area does not play a role in the problem. During backflow, the entire column of liquid would be pushed upstream. Letting v_1 be the initial Bernoulli velocity of the flow prior to the disturbance, we have

$$v_1 = \sqrt{\frac{2P_m}{\rho}} \tag{3.2}$$

Similarly, the Bernoulli velocity after the step change, v_2 is

$$v_2 = \pm\sqrt{\frac{2\,|P_m - P_2|}{\rho}} \tag{3.3}$$

Here v_2 takes the positive sign when $P_2 < P_m$. When $P_2 > P_m$, the flow reverses and takes on a negative value. Equation (3.1) is a nonlinear ordinary differential equation, that is integrated numerically to give instantaneous v and x values using an explicit second-order accurate in time method for computing velocity, v. This is done by expanding v using Taylor Series:

$$v^{(i)} = v^{(i-1)} + \frac{dv}{dt}^{(i-1)} \frac{\Delta t}{1!} + \frac{d^2v}{dt^2}^{(i-1)} \frac{\Delta t^2}{2!} + O\left(\Delta t^3\right) \tag{3.4}$$

Where i is the index for timestep. Equation (3.4) can be rearranged to make dv/dt the subject, followed by discretization:

$$\frac{dv}{dt}^{(i-1)} = \frac{1}{\rho L}\left(P_m - P_e^{(i-1)} \pm \frac{1}{2}\rho v^{(i-1)^2}\right) \tag{3.5}$$

The second-derivative term in Equation (3.4) can be discretized as follows:

$$\begin{aligned}\frac{d^2v}{dt^2}^{(i-1)} &= \frac{\frac{dv^{(i-1)}}{dt}-\frac{dv^{(i-2)}}{dt}}{\Delta t}\\ &= \frac{\frac{1}{\rho L}\left(P_m - P_e^{(i-1)} \pm \frac{1}{2}\rho v^{(i-1)^2} - P_m + P_e^{(i-2)} \mp \frac{1}{2}\rho v^{(i-2)^2}\right)}{\Delta t}\\ &= \frac{\frac{1}{\rho L}\left(-P_e^{(i-1)} + P_e^{(i-2)} \pm \frac{1}{2}\rho v^{(i-1)^2} \mp \frac{1}{2}\rho v^{(i-2)^2}\right)}{\Delta t}\end{aligned} \tag{3.6}$$

Substituting (3.5) and (3.6) into (3.4), we get the discretized form for the velocity of the liquid-gas interface:

$$\begin{aligned}v^{(i)} = v^{(i-1)} &+ \left(P_m - P_e^{(i-1)} \pm \frac{1}{2}\rho v^{(i-1)^2}\right)\frac{\Delta t}{\rho L}\\ &+\left(-P_e^{(i-1)} + P_e^{(i-2)} \pm \frac{1}{2}\rho v^{(i-1)^2} \mp \frac{1}{2}\rho v^{(i-2)^2}\right)\frac{\Delta t}{2\rho L} + O(\Delta t^2)\end{aligned} \tag{3.7}$$

Equation (3.7) is then integrated numerically in time to obtain the location of the interface which is also second-order accurate in time:

$$\begin{aligned}x^i &= x^{(i-1)} + \frac{dx}{dt}^{(i-1)}\frac{\Delta t}{1!} + \frac{d^2x}{dt^2}^{(i-1)}\frac{\Delta t^2}{2!} + \ldots\\ &= x^{(i-1)} + v^{(i-1)}\Delta t + \frac{v^{(i-1)} - v^{(i-2)}}{\Delta t}\frac{\Delta t^2}{2!} + \ldots\\ &= x^{(i-1)} + v^{(i-1)}\Delta t + \left(v^{(i-1)} - v^{(i-2)}\right)\frac{\Delta t}{2} + O(\Delta t^2)\end{aligned} \tag{3.8}$$

A grid sensitivity analysis was performed to ensure that the solutions obtained are independent of grid size. In this case, we want to ensure that the solutions are independent on the size of the timestep. This will be shown in the following sections when we look at cases where an injector is subjected to a step change in downstream pressure, as well as a triangular pressure pulse.

3.1.1 Response to a Step Change in Downstream Pressure

The orifice transit time τ represents a fundamental quantity in describing the dynamic response of the column:

$$\tau = \frac{L}{v_1} \tag{3.9}$$

We can also define a dimensionless pressure $p=P_m/P_2$ that characterizes the strength of the imposed disturbance relative to the manifold pressure. Consider the case when $P_1=0$ at $t<0$ and $p=P_m/P_2$=constant when $t>0$. This represents a step pressure change which drives the fluid flow to a different steady state. We can define a response time t_r, as the time taken for the flow to reach 95% of the difference between v_1 and v_2 since an asymptotic behavior is expected as the flow approaches v_2 and the driving acceleration becomes diminished.

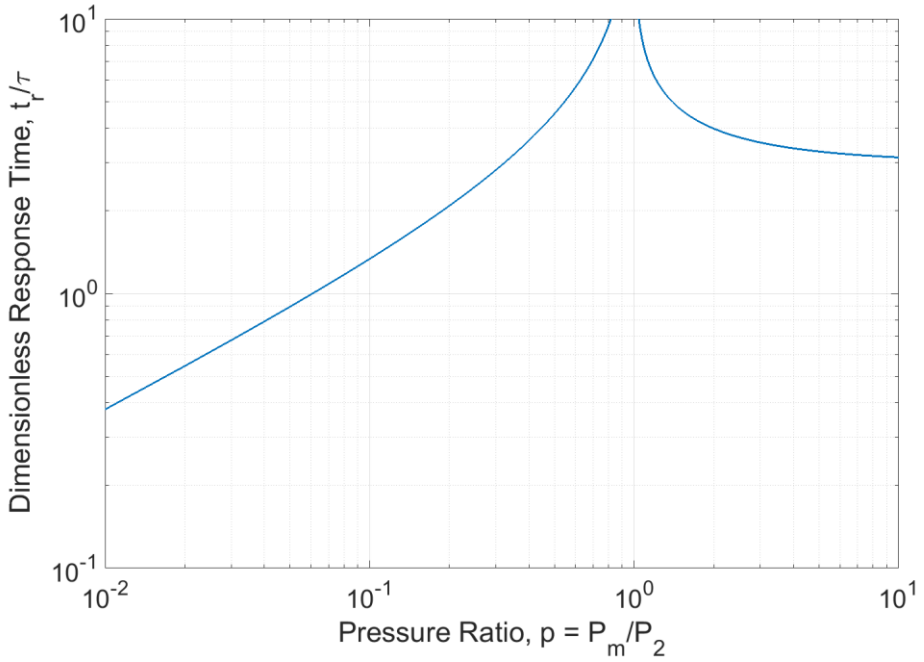

Figure 3-2. Plot of non-dimensional response time vs. non-dimensional manifold pressure ratio.

Figure 3-2 depicts the behavior of this response time over a wide range of pressure disturbance amplitudes. When $p>>1$ the imposed disturbance is a small fraction of the initial manifold pressure and the response time tends to asymptote to $t_r \approx 3\tau$ under these conditions. For a very strong disturbance such as that imparted by a detonation wave $p<<1$ and the most rapid response is attained under these conditions with $t_r<2\tau$. When very weak disturbances are imposed ($p \approx 1$) the orifice takes the longest to respond since the imposed forces are the smallest under these conditions.

When $p<1$ the column moves backward toward the manifold as the imposed downstream pressure exceeds the manifold pressure. Integrating the velocity history, we can determine the time required for the flow to traverse the entire length of the passage, i.e. when $x=-L$. Here we remind the reader of the constant column mass assumption; when substantial backflow occurs one might envision the effective column mass/inertia being reduced. For this reason, one might regard results from this simple integration to be upper bounds on the backflow time t_b. Figure 3-3 depicts the time to backflow as a function of the disturbance amplitude p. Here, we note that the backflow time is follows a very similar profile to that of response time within the same range of p. Detonation pressure ratios can exceed 20-30 for some propellants – under these conditions the entire orifice would backflow under a fraction of an orifice transit time τ. The response time has also been plotted on the same graph and it can be seen that response and backflow times are almost the same, implying that the flow attains its final velocity just as the free surface reaches the manifold. While instructive, these results are of limited practical use since detonation events are highly transient, characterized by a steep-fronted pressure spike followed by a period of pressure decay.

For this reason, we consider a sawtooth-shaped pressure disturbance characterized by instantaneous rise to a maximum pressure P_2 followed by a linear decay in pressure as a disturbance more representative of passage of a detonation wave.

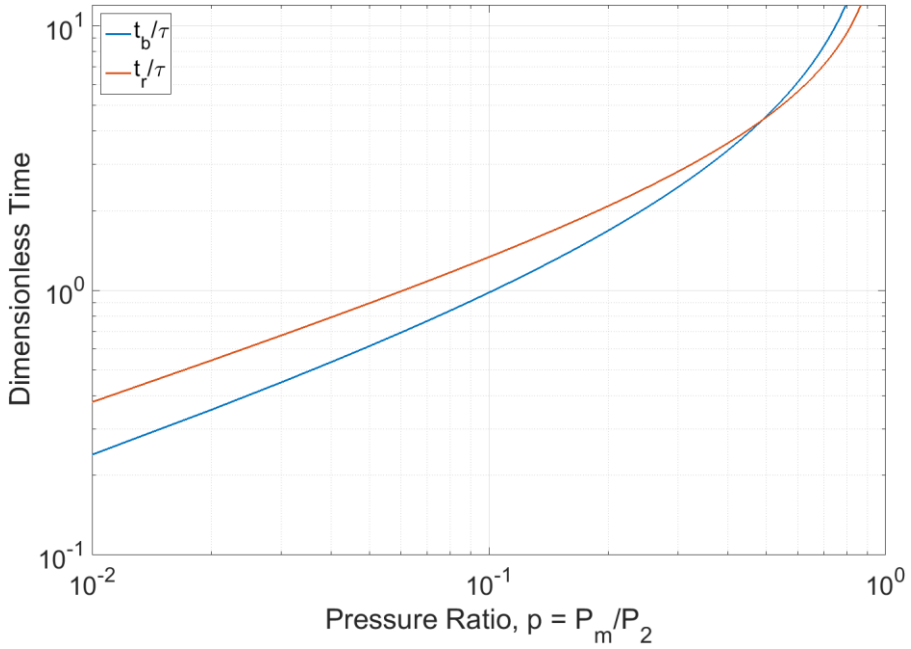

Figure 3-3. Plot of non-dimensional backflow time and non-dimensional response time vs. non-dimensional manifold pressure ratio.

3.1.2 Response to a Sawtooth Profile in Downstream Pressure

Existing literature suggests that detonation decay times τ_c are of the order of 50-70μs[13,14]. A 1 cm long orifice with injection velocity of 50 m/s gives an orifice transit time of 200μs. While seemingly short, the large detonation wave speed produces operating periods in a RDE that are comparable to these times. For example, Purdue's operational RDE test combustor whose channel diameter is approximately 10cm produces detonations whose periods are of the order of 125μs. It becomes immediately apparent that the injector spends a large portion of the total operational period under dynamic response and has an exceedingly short time after recovery to achieve the required fill height. Under strong detonation conditions a steady state may never be achieved. As such, it is of utmost importance to be able to tune its parameters as precisely as possible.

If we let τ_c be the time taken for the pressure spike to decay, we non-dimensionalize and replace the P_e term in equation (3.1) with

$$\frac{P_e(t)}{P_2} = \begin{cases} 1 - \dfrac{t}{\tau_c} & 0 < t \le \tau_c \\ 0 & otherwise \end{cases} \tag{3.10}$$

Here P_2 is the peak amplitude of the sawtooth wave. Equation (3.10) can be integrated in time for this imposed disturbance in order to assess dynamic response for this signal. The total impulse applied to the column for this triangular wave is simply $I=P_2\tau_c/2$. Parametrically, we can consider the effect of the decay time τ_c while keeping P_2 constant, or we can consider a fixed total impulse and vary P_2 and τ_c to assess the influence of the shape of the pulse. As before, we can define a response time t_r, in this case as the time taken for the liquid to return to 95% of its initial velocity following the pressure event.

3.1.2.1 Effect of Decay Time

Figure 3-4 depicts three different triangular pulses of constant maximum strength and varying decay times. Equation (3.5) is integrated numerically for these pulses in order to assess the orifice dynamic response. Figures 3-5 and 3-6 depict the dimensionless velocity and column exit position histories. Since the initial disturbance pressure is the same for all cases, the initial deceleration in Figure 3-5 is approximately constant for all five decay times. Since longer pulses imply a larger total impulse applied to the column, the minimum velocity goes lower and overall recovery time grows longer as the pulse duration is lengthened. Figure 3-6 provides an insightful demonstration that the flow does not necessarily backflow even when P_2 is an order of magnitude greater than P_m, and that the total impulse also needs to be considered. The initial momentum in the moving column is sufficient to negate backflow until a certain level of impulse is achieved.

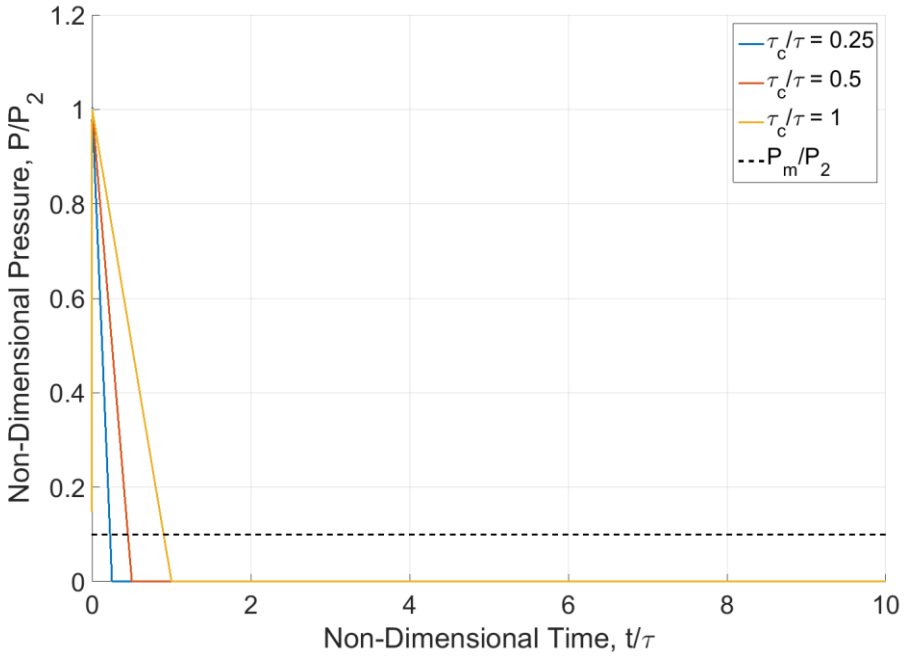

Figure 3-4. Plot of pressure profiles with constant peak pressure and varying decay times.

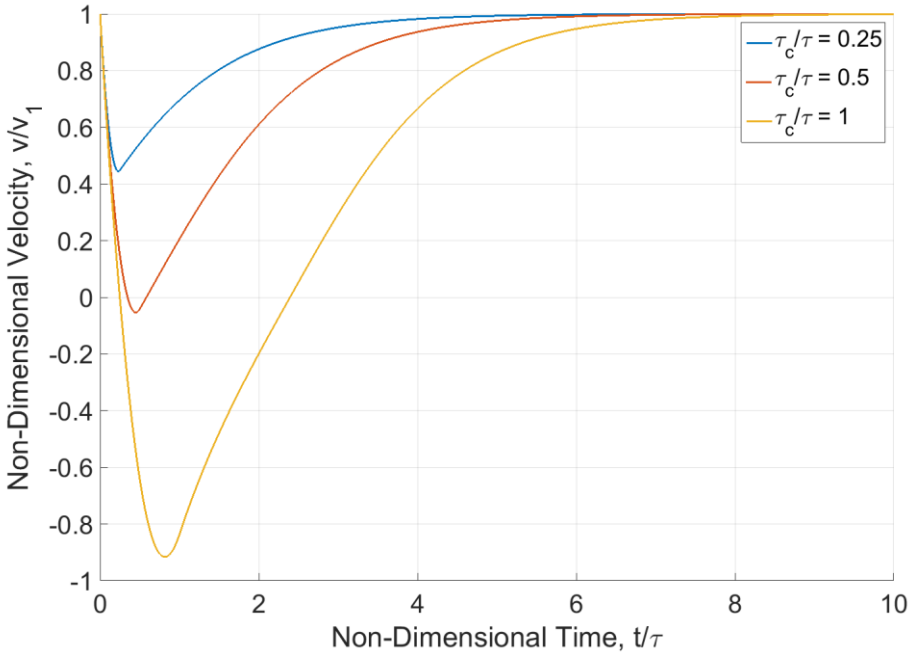

Figure 3-5. Plot of non-dimensional velocity vs. non-dimensional time for various decay times. P_m/P_2=0.1.

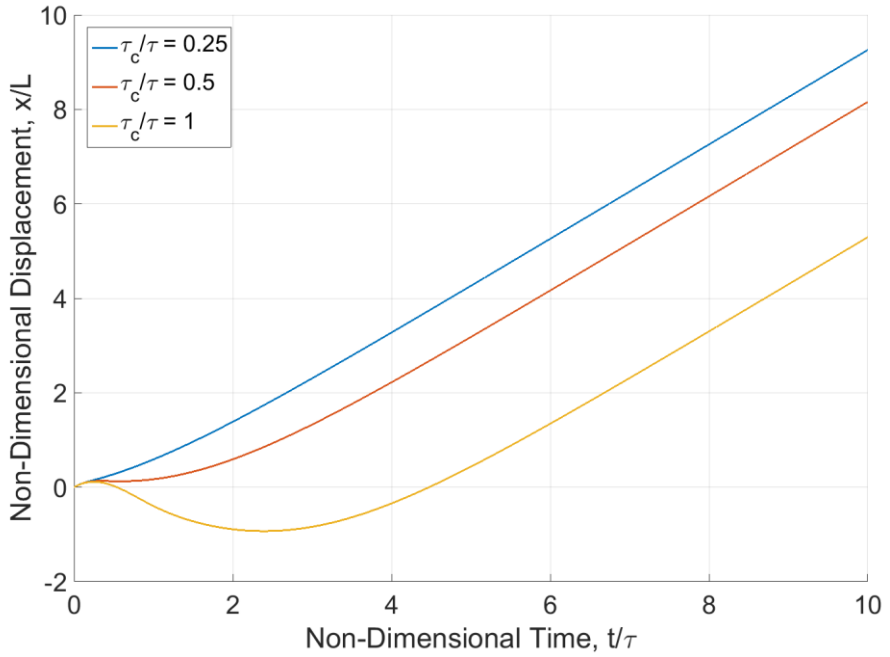

Figure 3-6. Plot of non-dimensional displacement vs. non-dimensional time for various decay times. P_m/P_2=0.1.

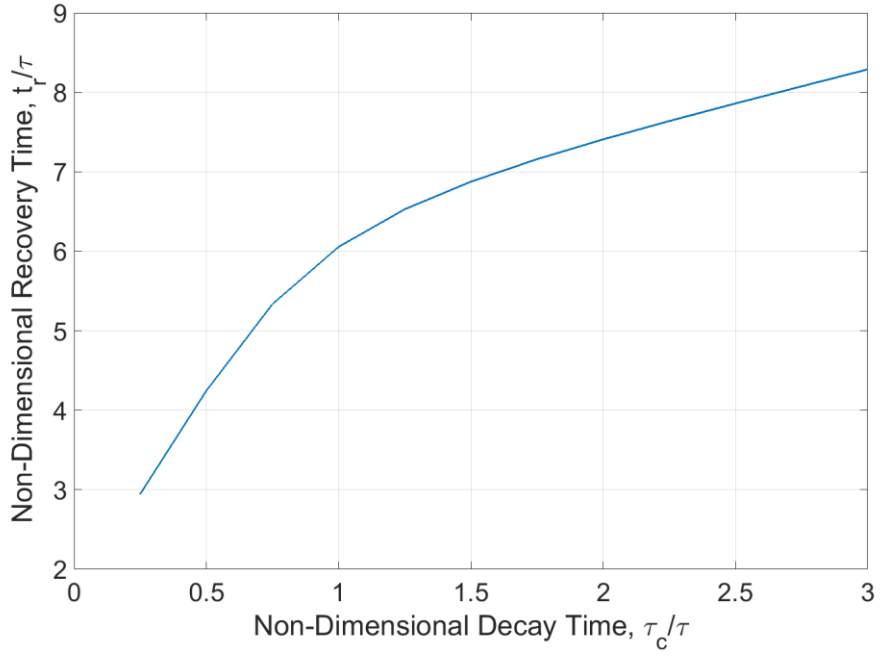

Figure 3-7. Plot of non-dimensional recovery time vs. non-dimensional decay time. P_m/P_2=0.1.

Figure 3-7 shows that the recovery time is typically several times longer than the decay time of the pressure wave indicating that the memory of the imposed impulse is significant. This result is very important for detonation engine combustion dynamics as it implies that the propellant mass flow rate is slow to recover relative to the pressure decay, and that sufficient time must be allowed before the arrival of the next pressure wave if performance is to be maintained. In order to achieve high dynamic orifice response, one must minimize τ itself as all the dynamic response characteristics tend to scale with this parameter.

3.1.2.2 Effect of Disturbance Amplitude under Constant Impulse Conditions

Here, constant total impulse is considered. Setting P_m to be a constant value across all cases, P_2 is defined as $10P_m$ so that a baseline case is established using $\tau_c/\tau=1$, $P_e/P_2=1$. The peak pressure for other cases is computed assuming $I=P_2\tau_c/2$. Figure 3-8 shows the resulting waveforms under this assumption.

Figures 3-9 and 3-10 show velocity and position histories for the waveforms in Figure 3-8. In this case, Figure 3-9 shows varying degrees of initial deceleration since the peak pressure is now different for each of the cases. While there is a more violent velocity excursion for a high amplitude short pulse as compared to a low amplitude long pulse, the asymptotic behavior and overall response time varies little for the cases considered. This is a fundamental result that is important to system dynamics as the shape of the imposed overpressure is of less concern than the overall impulse applied to the system. Figure 10 reinforces this notion in terms of the location of the end of the column. Once the imposed impulse has been applied, all the cases tend to asymptote to the same overall system response.

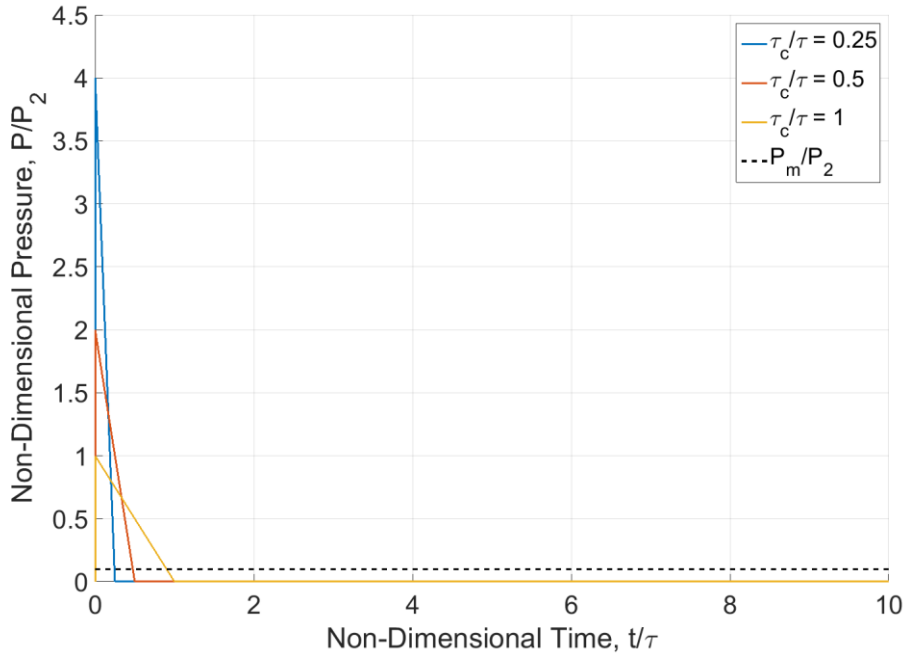

Figure 3-8. Plot of pressure profiles with constant total impulse.

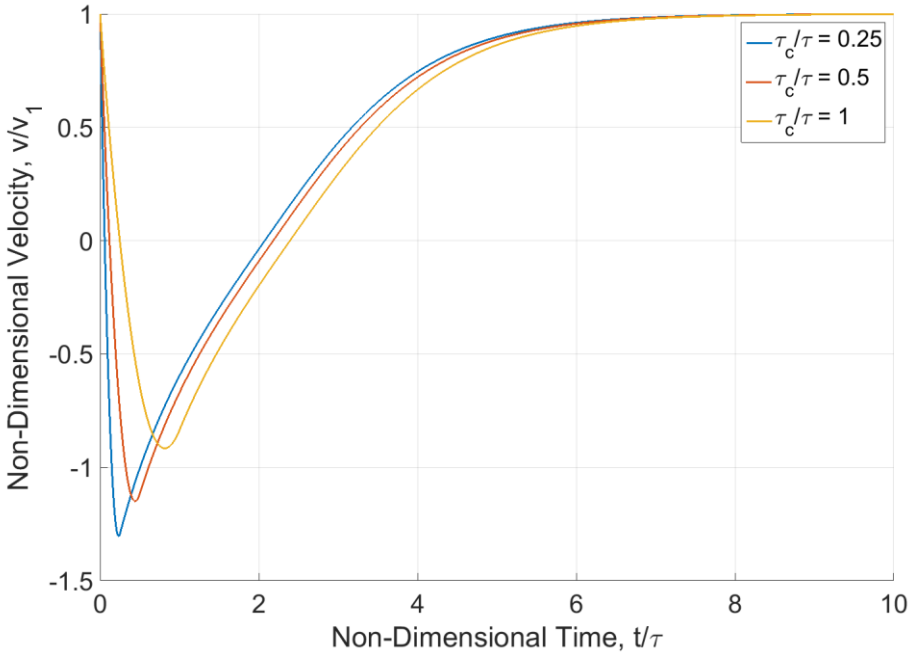

Figure 3-9. Plot of non-dimensional velocity vs. non-dimensional time for various decay times and peak pressures.

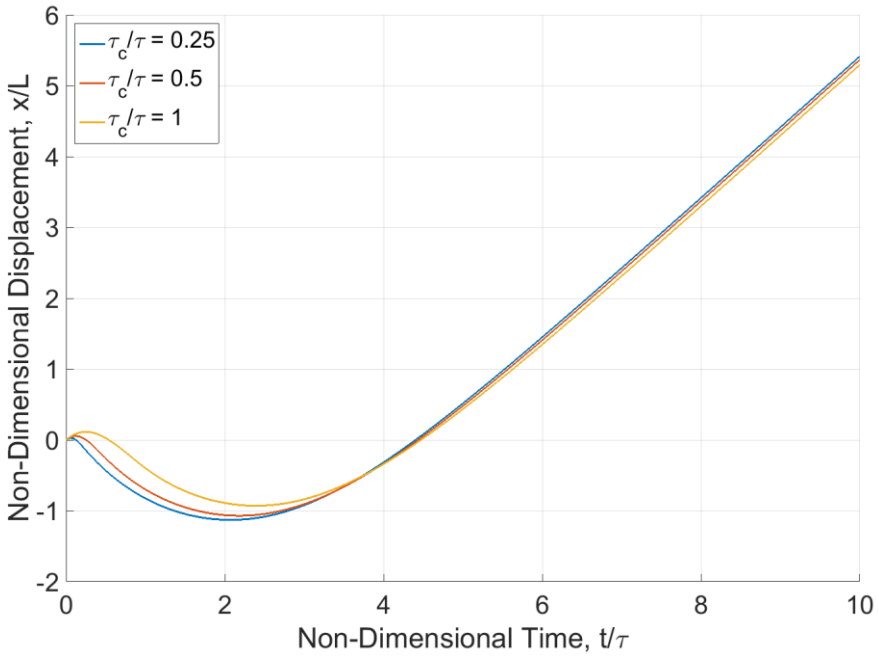

Figure 3-10. Plot of non-dimensional displacement vs. non-dimensional time for various decay times and peak pressures.

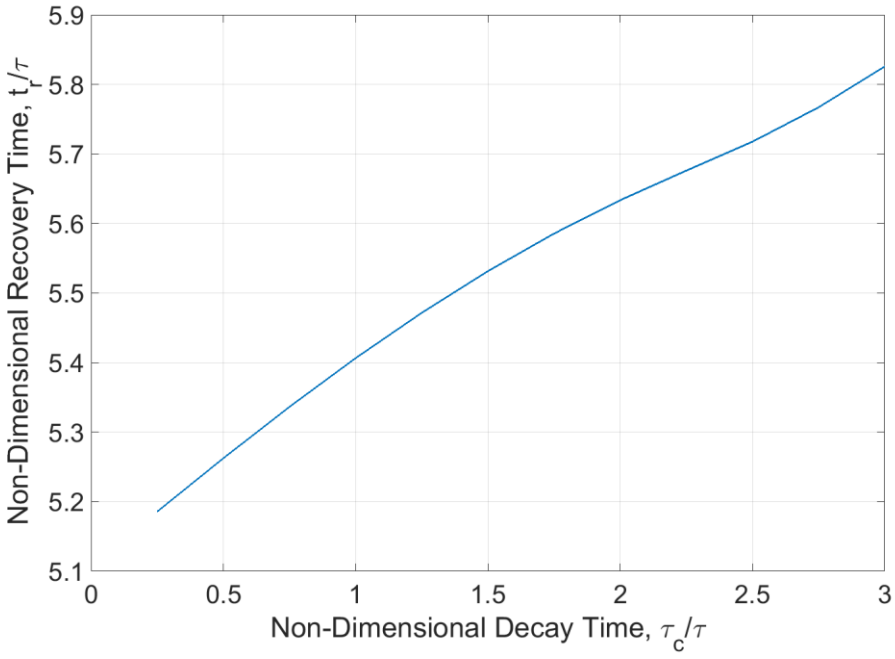

Figure 3-11. Plot of non-dimensional recovery time vs. non-dimensional decay time.

Figure 3-11 depicts the overall recovery time for the waveforms in Figure 3-8. Results show only small variation in recovery time over the range of conditions considered. To first order, one might assess the orifice dynamic response based solely on the impulse generated by the wave.

3.1.3 Timestep Sensitivity Study

To ensure that discretization error is minimized, a timestep sensitivity study was performed for the numerical analysis presented above. Figures 3-12 through 3-17 show plots of velocity and interface location vs. time for three different time steps overlaid on the same graph. Figures 3-12 through 3-15 represent cases where $p=0.1$ and Figures 3-16 and 3-17 are for $p=0.025$. For all cases, $\tau_c/\tau=0.25$ presents the steepest change in pressure with time while $\tau_c/\tau=1.0$ results in the largest disturbance in interface location for the case where peak amplitude was kept constant. Under these conditions, numerical treatment becomes the most sensitive and these parameters were therefore chosen as the benchmark for the sensitivity analysis.

In all the figures, the plots for $\Delta t=1e\text{-}8$ and $\Delta t=1e\text{-}9$ overlap each other while that of $\Delta t=1e\text{-}7$ lies a visible distance away. This shows that the solutions of the fixed-mass analysis shown above, computed using $\Delta t=1e\text{-}8$, have converged and further reduction in timestep size would have minimal effect on the solution.

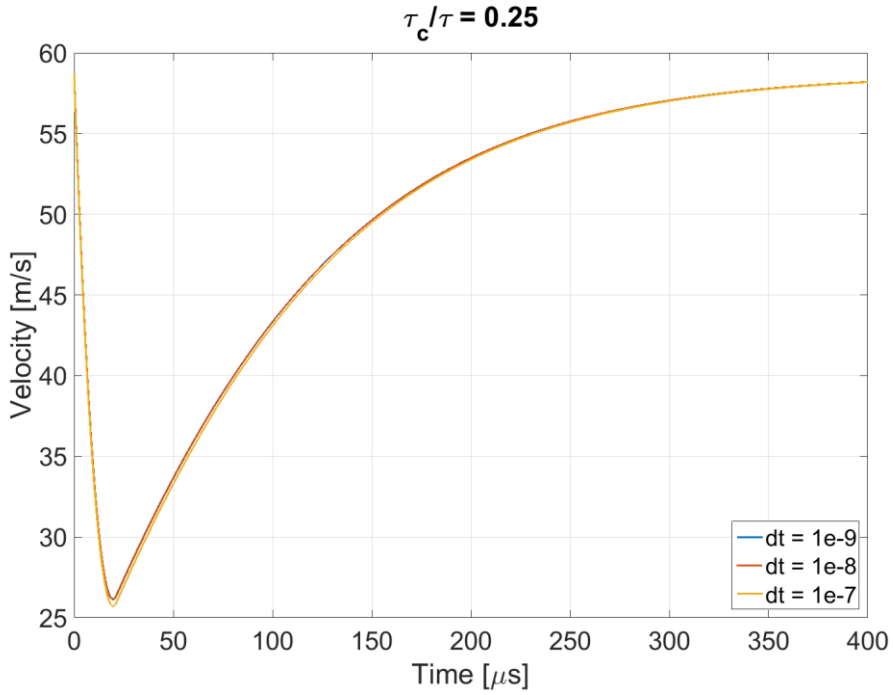

Figure 3-12. Plot of interface velocity vs. time showing solution convergence at timestep Δt=1e-8s for τ_c/τ=0.25.

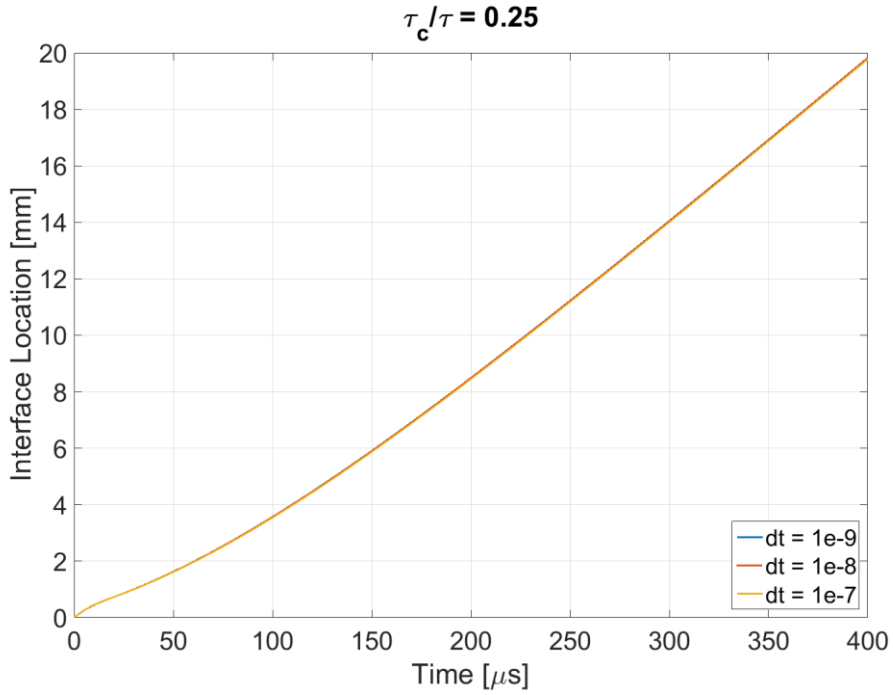

Figure 3-13. Plot of interface location vs. time showing solution convergence at timestep Δt=1e-8s for τ_c/τ=0.25.

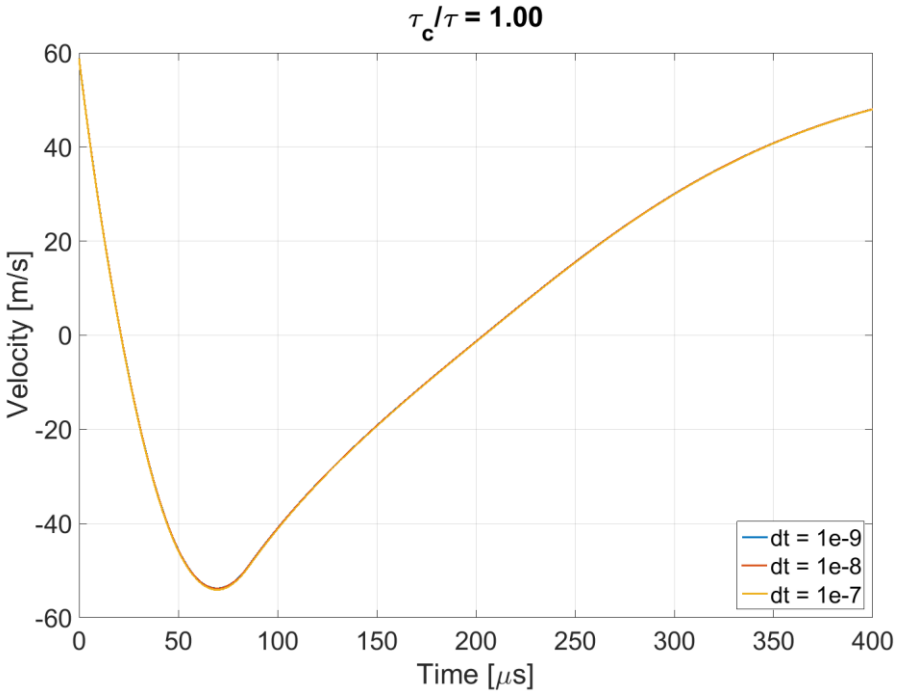

Figure 3-14. Plot of interface velocity vs. time showing solution convergence at timestep Δt=1e-8s for τ_c/τ=1.00.

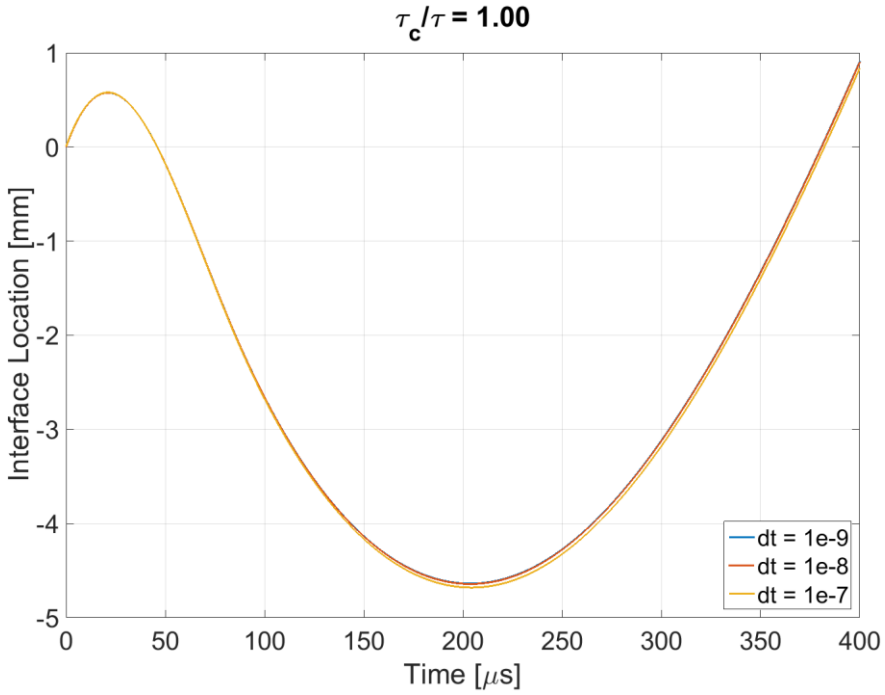

Figure 3-15. Plot of interface location vs. time showing solution convergence at timestep Δt=1e-8s for τ_c/τ=1.00.

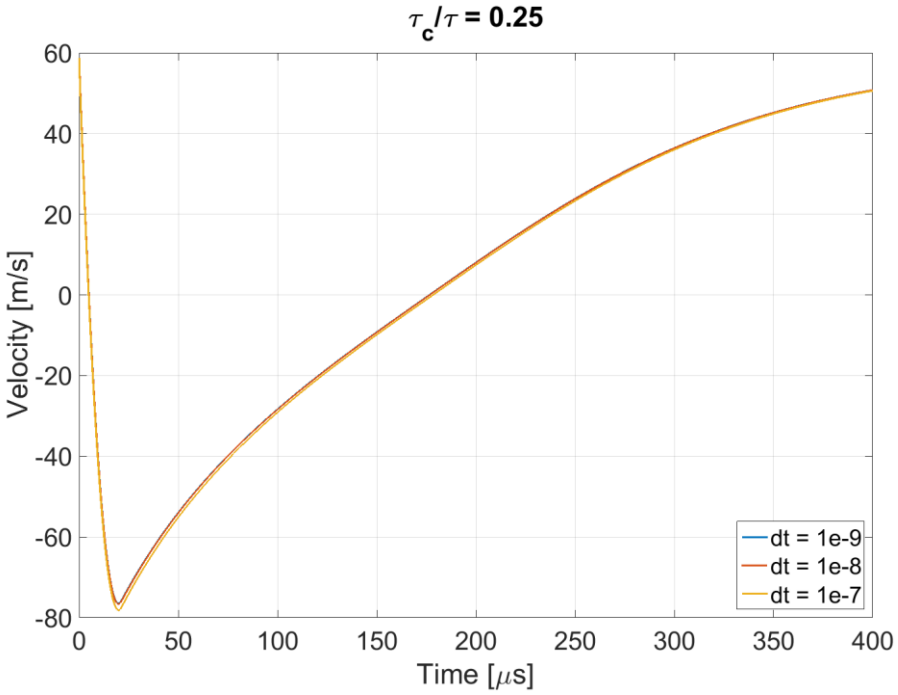

Figure 3-16. Plot of interface velocity vs. time showing solution convergence at timestep Δt=1e-8s for τ_c/τ=0.25.

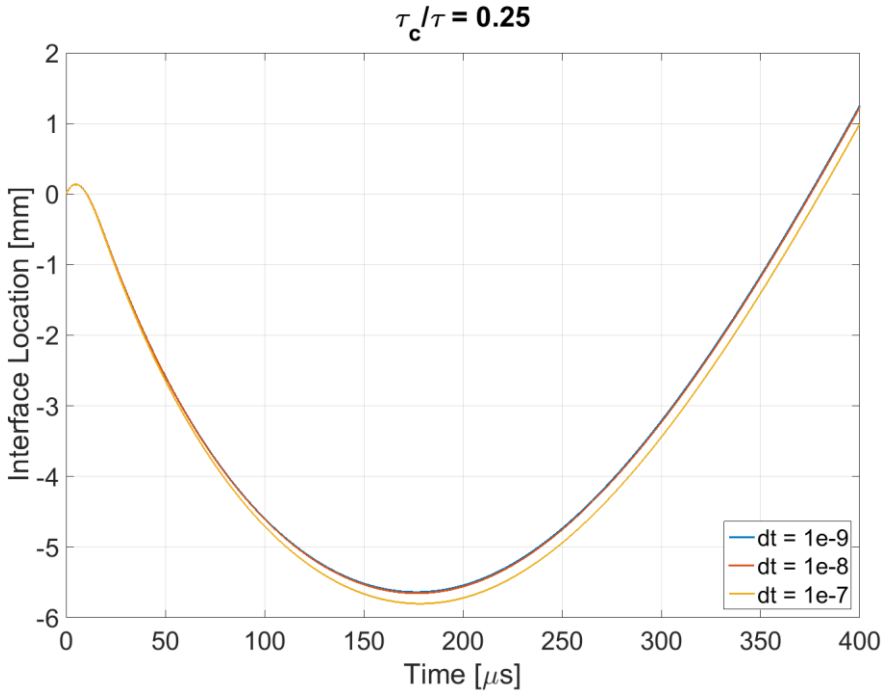

Figure 3-17. Plot of interface location vs. time showing solution convergence at timestep Δt=1e-8s for τ_c/τ=0.25.

3.2 Variable-Mass Model

While the fixed mass analysis highlighted some top-level characteristics of importance, a more accurate representation of the system was desired. A relaxation on the fixed mass constraint and inclusion of viscous effects gave rise to a variable-mass model for the injector. At the same time, the previously mentioned negligence of flow boundaries beyond the inlet and exit of the injector were also addressed by freezing *x* at 0 or L when it exceeds those values. The constant injector cross section and rigid body assumptions are retained for this analysis. As before, given a chamber pressure signal, injector manifold pressure, and injector length as inputs, the model calculates the acceleration acting on the liquid column based on the pressure gradient across the injector. Numerical integration of acceleration in time results in the velocity of the liquid-gas interface and a second integration in time gives its position. The model begins with the same equation (3.1). It can be rewritten with acceleration as the subject as

$$a_{pg} = \frac{1}{\rho_{avg} L}\left(P_m - P_e \pm \frac{1}{2}\rho_{avg} v^2 \right) \tag{3.11}$$

Here, the density is the mass weighted average of the liquid and gas present in the orifice. It is important for the combusted gas density to be accounted for here so that when the entire injector is filled with combustion products, the equation does not involve a division by zero.

In real flow, frictional loss is expected on the channel wall and is calculated using the Fanning friction factor, *f*:

$$f = \frac{16}{Re}, \; Re \le 2100 \tag{3.12}$$

$$\frac{1}{\sqrt{f}} = -4.0 log_{10}\left(\frac{\varepsilon}{3.7D} + \frac{1.256}{Re\sqrt{f}} \right), \; Re > 2100 \tag{3.13}$$

where $Re = \rho v D/\mu$ is the Reynolds number. The Colebrook equation[15] for turbulent regime requires f to be solved numerically. After f is obtained, wall shear stress is computed, followed by wall shear force.

$$S = \frac{1}{2} f \rho v^2 \tag{3.14}$$

$$F_{fric} = SA_{wet} \tag{3.15}$$

where v is the interface velocity. It is important to note that the equation requires the Fanning, and not the Darcy, friction factor. Friction of only the liquid is considered here since its density and viscosity are much greater than those of the gaseous combustion product. The mass of liquid in the orifice is then the product of the orifice cross section, liquid column length, and liquid density. The mass of the fluid in the injector channel is given by

$$m = \frac{\pi D^2 x \rho_{avg}}{4} \tag{3.16}$$

The net acceleration of the liquid column is the sum of the acceleration due to pressure gradient and the deceleration due to friction:

$$a_{net} = a_{pg} - \frac{F_{fric}}{m} \tag{3.17}$$

Numerical treatment in the variable mass model remains the same as that shown for the fixed mass model in Section 3.1. The timestep employed in all cases is 1×10^{-9}s. While the fixed-mass analysis used simple waveforms as pressure input, the actual empirical pressure data will be used here so that a comparison can be made between the predicted and actual injector response. Plots of numerical solutions will be presented in Chapter 4 alongside empirical data for this purpose.

CHAPTER 4. RESULTS AND ANALYSIS

Figure 4-1 shows a macroscopic view of events as a detonation wave travels down the channel. The wave travels from top to bottom and water flows from left to right. The water jet is seen here to get rapidly broken up into a fine mist by the blow down of combustion gas. At the same time, the column of water in the injector can be seen getting pushed back towards the plenum by the sudden spike in pressure. This series of images taken at 12,000 frames per second (fps) and 304 by 512 pixels resolution serves to provide an overall picture of the events during each test run. Subsequently, the viewing window was reduced significantly to allow the camera to run at higher (more than 80,000) frame rates so that more details of the injector's response can be captured.

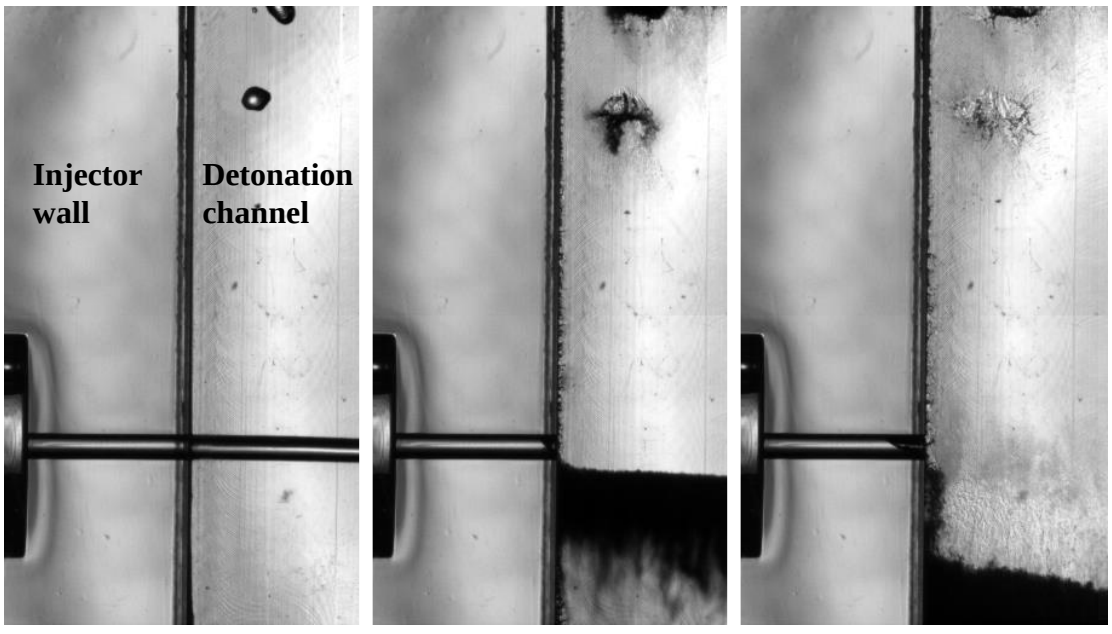

Figure 4-1. Macroscopic view of events during a typical test run. Pressure wave travels from top to bottom and liquid flow is from left to right. Recorded at 12,012fps and 304 by 512 pixels resolution.

4.1 Pressure Data

Almost all of the pressure data obtained showed characteristic double peaks during the passage of the pressure wave. Figure 4-2 shows a typical pressure trace obtained during the experiment. A majority of them were followed shortly after by a large amplitude, long duration pressure excursion which is attributed to thermal drift from gauge exposure to the hot combustion gases. Two major evidences support this hypothesis, the first being that the amplitude and duration of the events do not match the behavior of the liquid seen in the videos. The amplitude of the excursion is often in the region of 100psia, lasting approximately 1.5ms. Videos show that the injectors have usually recovered well before the pressure amplitude has fallen below manifold values. Secondly, these pressure excursions are not present in the pressure data for Design L (Figure 4-3), whose pressure transducer was situated directly across the injector, resulting in direct impingement and accumulation of water over the transducer. It is likely that the presence of the water film on the transducer face mitigated the heat transfer from the hot gas into the transducer. Furthermore, Figure 4-4 shows convincing evidence that the excursions were caused by thermal drift of the pressure transducer. Here, the second peak of the pressure wave is seen to have been dislocated to the top of the pressure excursion.

The contamination of the pressure information by thermal drift posed a challenging problem for the study whose objective includes the validation of the dynamic response model as the drift often corrupted the event we were trying to capture. Of the 75 sets of data collected for the three designs, 23 of them were free of thermal drift during the impulse provided by the detonation wave. Figure 4-5 is the result of overlaying all 23 pressure traces on the same plot. Signal spikes appearing before approximately 2.5×10^{-3}s are artifacts from the spark plug's electrical noise. As can be seen, most of the traces show very similar peak amplitudes and pulse duration. Additionally, the double peak regions of most of the contaminated traces also follow the same form. Therefore, it is reasonable to assume that the pressure waves in all experiments were of similar strength and duration.

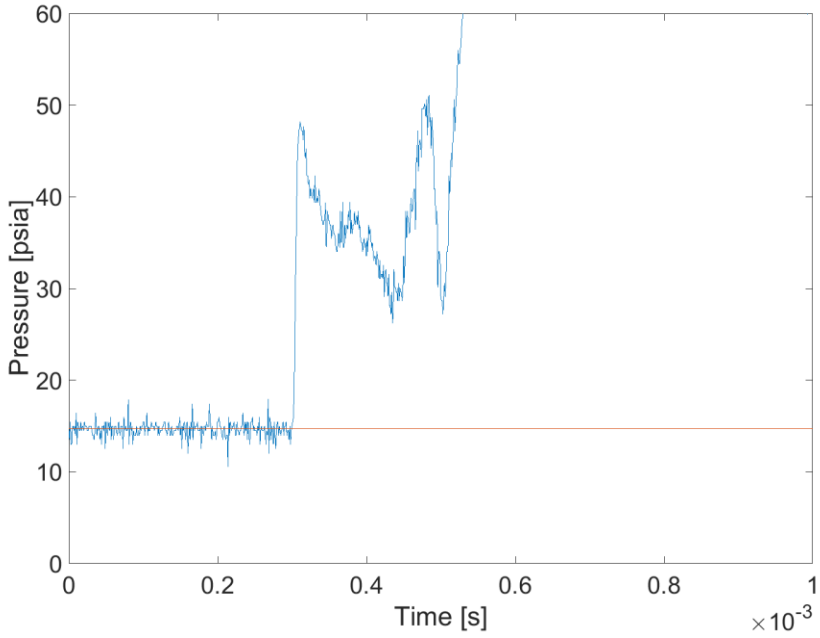

Figure 4-2. Typical pressure trace recorded during tests using designs M, S and P. Red line represents atmospheric pressure of 14.7 psia.

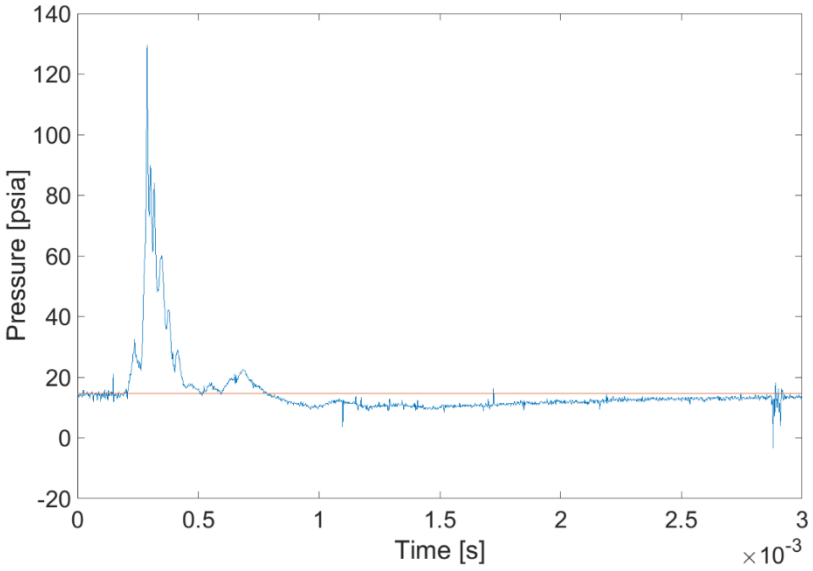

Figure 4-3. Typical pressure trace recorded during tests using design L. Red line represents atmospheric pressure of 14.7 psia.

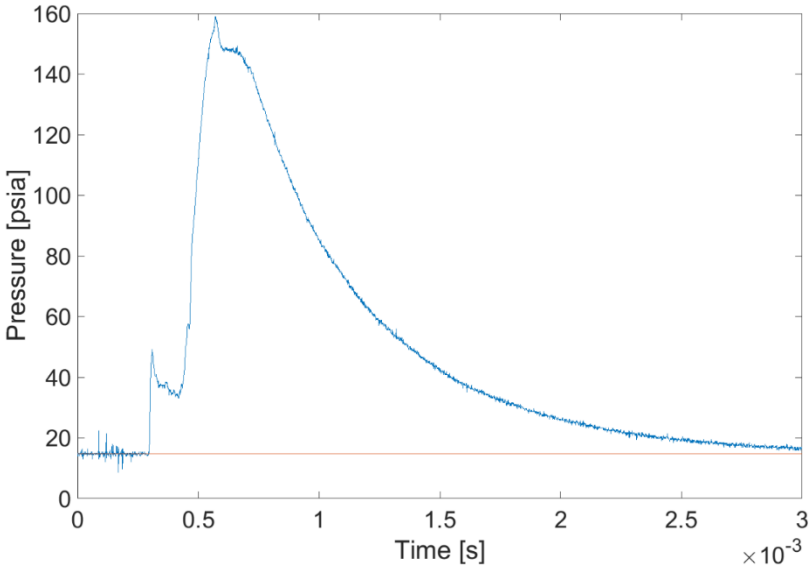

Figure 4-4. Pressure trace supporting explanation of large-amplitude pressure excursion resulting from thermal drift.

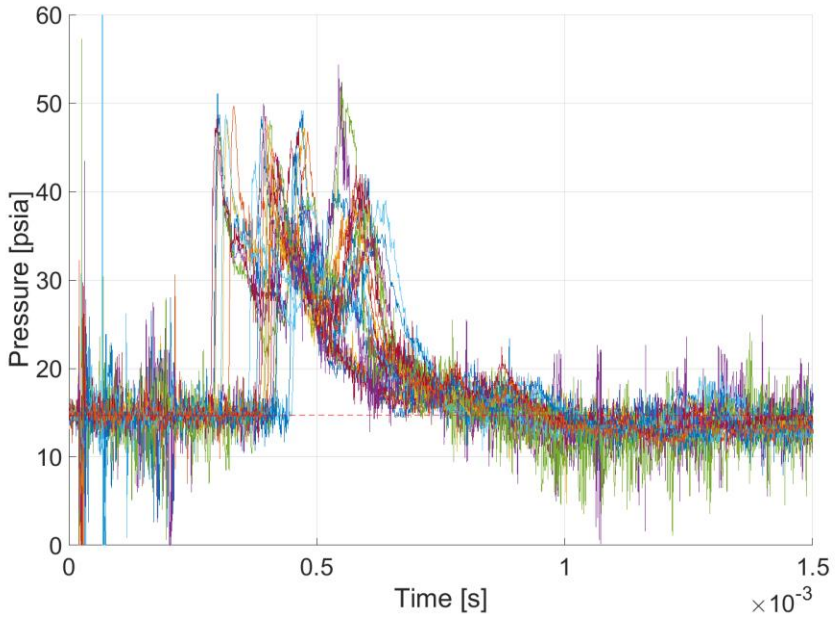

Figure 4-5. Overlay of 23 pressure traces with minimal thermal drift showing consistency of measurements.

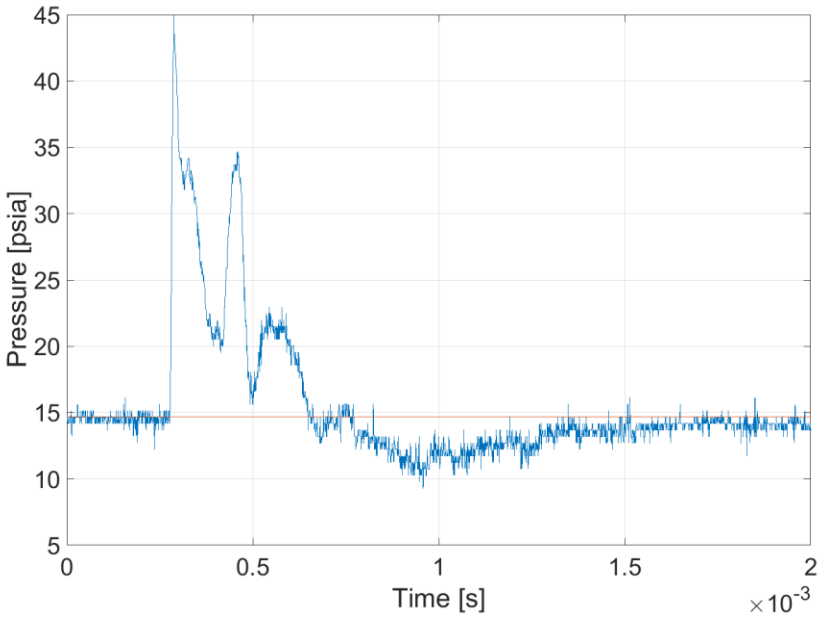

Figure 4-6. Representative pressure trace used as input for numerical model. Thermal drift is still visible here but is of small amplitude and short duration.

4.2 Qualitative Image Analysis

Figure 4-7 through Figure 4-9 below are sequenced still images extracted from the videos showing the three different types of response observed. The images have been rotated 90° counterclockwise from the original orientation for formatting reasons. The detonation channel is at the top of the images and the injector plenum is at the bottom. Injection direction is from bottom to top. The detonation wave traverses the injector face from left to right.

The results of the experiments can be classified under three broad categories: complete backflow, partial backflow, and limited backflow. Complete backflow is defined by gaseous combustion products penetrating the entire length of the orifice and becoming trapped in the plenum. Partial backflow occurs when the gas/liquid interface propagates upstream into the orifice passage. Finally, limited backflow is characterized by the case where gas occupies just a portion of the orifice cross section near the exit

plane. The absence of inversion of the liquid-gas interface is also a characteristic of limited backflow. Examples of each category are shown in the figures that follow.

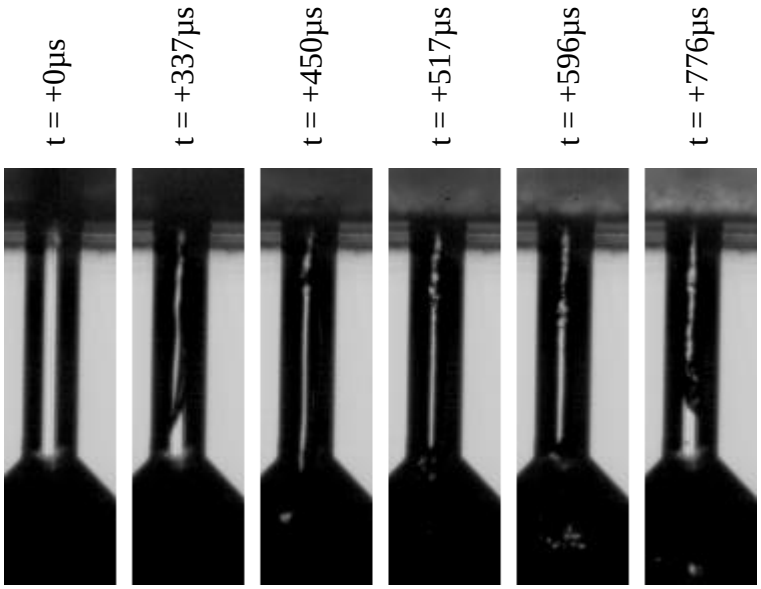

Figure 4-7. Sequence of images from left to right showing combustion gas penetrating into injector plenum. Detonation wave travels from left to right and liquid flows from bottom to top. Recorded at 88,888fps and 208 by 56 pixels resolution.

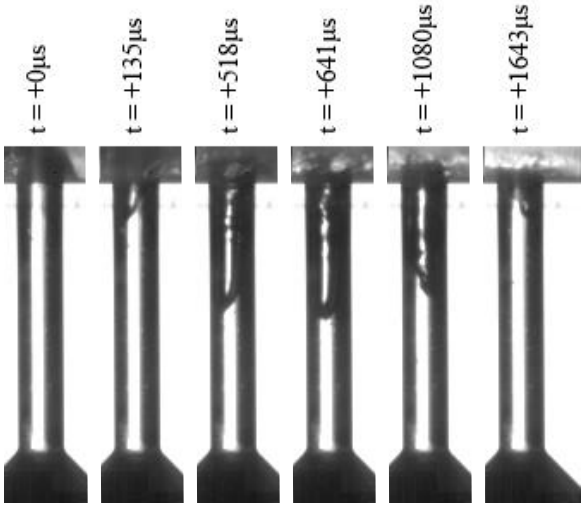

Figure 4-8. Sequence of images from left to right showing partial injector backflow. Detonation wave travels from left to right and liquid flows from bottom to top. Recorded at 83,33fps and 240 by 56 pixels resolution.

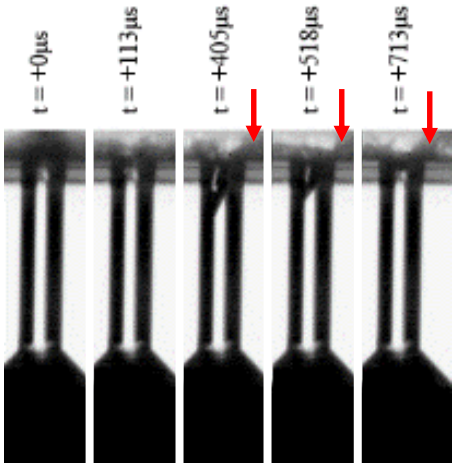

Figure 4-9. Sequence of images from left to right showing limited backflow at high injector pressure gradient. Detonation wave travels from left to right and liquid flows from bottom to top. Recorded at 88,888fps and 208 by 56 pixels resolution.

Under very low-speed liquid injection conditions, combustion gases propagate up the injector passage all the way into the injection plenum as illustrated in Figure 4-7 (i.e. a complete backflow situation). Gas first enters the injector passage through the boundary layer on the upwind side of the orifice. For this reason, the liquid-gas interface appears tilted toward the upwind side of the injector passage. For the test shown in Figure 4-7, the interface moves the entire length of the injection passage in about 300 microseconds with an average velocity of 12.7m/s. Upon penetration into the orifice plenum, some of the gas remains trapped in the plenum as the bubble column collapses from the density difference with the surrounding liquid. The period between 450 and 517µs in Figure 4-7 is presumably a time when there is nearly no liquid in the orifice passage except for a small annular liquid region along the wall of the orifice, evident from the visible distortion close to the exit plane. At 517µs, liquid surrounding the previously continuous column of gas pinches off the column at the orifice entrance and forms a new free surface. At 596µs the free surface becomes more visible as recovery begins. Note that in the last frame the liquid-gas interface is now tilted toward the downwind side of the orifice passage; presumably the upwind side of the passage recovers first during this highly transient process. The conditions in Figure 4-7 only occur at very low water feed pressures, but are

obviously undesirable for operation of an engine as combustion gases make their way into propellant manifolds.

Figure 4-8 depicts partial backflow that could presumably occur if a low/intermediate liquid feed pressure (soft injection system) is employed. As with the large backflow condition in Figure 4-7, the liquid-gas interface is tilted toward the upwind side of the injector and the interface inverts its tilt as flow recovers and liquid pushes out the two-phase region. This interesting behavior appears consistently in the results and appears to be a fundamental multidimensional effect. One can imagine the high pressure gas first pushing into the upwind boundary layer in the orifice, leading to a tilted free surface. Similarly, during recovery phases it is the downwind side of the orifice passage that last sees the high pressure gas condition and therefore might cause a delayed recovery relative to the upwind side of the passage. It is surprising that this multidimensional argument appears to hold even when the free surface is pushed a substantial distance upstream into the orifice passage. Here the backflow duration is of the order of 400-500 microseconds. Flow recovery appears to occur over a similar time interval.

In the final series of images in Figure 4-9, limited backflow has occurred. Here the manifold pressure was sufficiently high to prevent the injector from checking off completely; this behavior might be characterized as a “stiff” injection system. The arrows indicate continued liquid flow from the downwind region of the orifice even while other portions of the orifice were undergoing backflow. These dynamics tend to be more readily apparent in the video playback. The third image (middle) shows the injector in a state of backflow and the fourth shows it in the process of recovery. In both of these imagines, the slope direction of the liquid-gas interface remained the same, i.e. this inversion of the tilting of the surface tends not to occur under these higher feed pressure conditions.

4.3 Quantitative Measurements from Video Data

Video data were analyzed to obtain backflow distance and time taken between the arrival of the detonation wave and refilling of the orifice of liquid. The backflow distance was chosen to be the maximum displacement of the liquid-gas interface observed along the centerline of the injector and refill time was defined as the time between the first observable arrival of the pressure wave and complete refilling of the injector with liquid. It must be mentioned at this point that during limited backflow, portions of the orifice continue to flow in the positive direction (into the detonation channel) and as a result, backflow distance cannot be easily defined or measured meaningfully. However, to maintain consistency, it was measured along the centerline as well for these cases.

Measured backflow distance x_b was non-dimensionalized by injector length L, and measured refill time t_r by orifice transit time τ. These were plotted against pressure drop ΔP across the injector, non-dimensionalized by manifold pressure P_m.

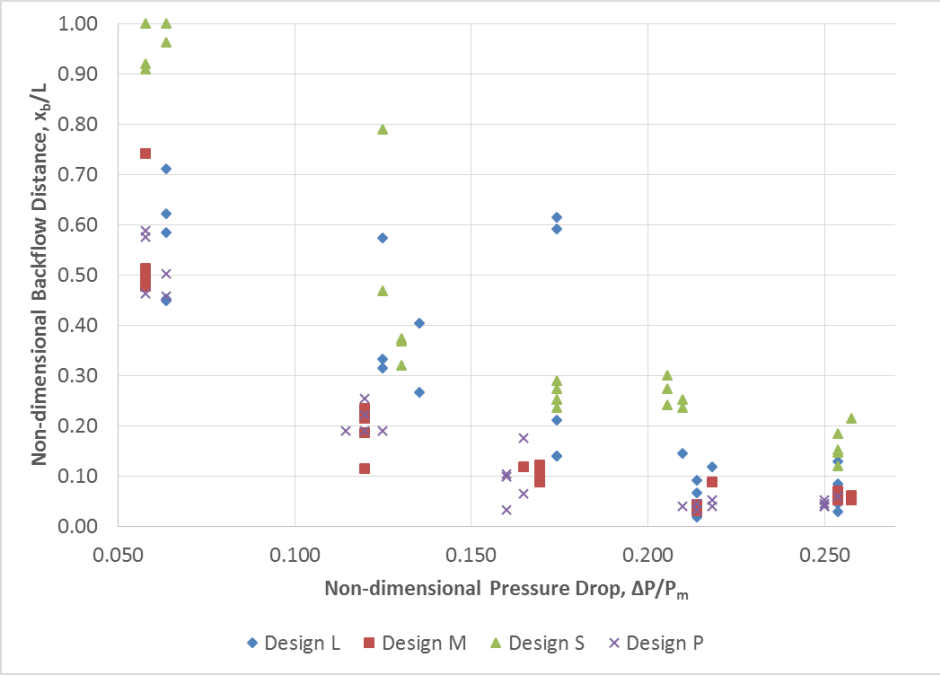

Figure 4-10. Plot of non-dimensional backflow distance vs. non-dimensional pressure drop across injector.

Figure 4-10 shows the non-dimensional backflow distance plotted against non-dimensional pressure drop. A relatively large scatter is seen in Design L, especially where $\Delta P/P_m \approx 0.17$. This was likely due to the obstructed flow passage mentioned in Chapter 2. All designs exhibit a nonlinear relation between backflow and pressure drop. However, no further detail of the relation could be inferred because of the dissimilar curve profiles across designs. On a different note, it is worth mentioning that reducing the plenum cross section in Design P drastically reduced the amount of backflow compared to Design S even though the increased dynamic pressure of the reduced cross section only amounted to less than 0.7% of the manifold pressure at its maximum. This suggests that the interactions among the backflowing liquid jet, the surrounding liquid in the plenum, and plenum walls play an important role in influencing the injector's resistance to back pressure. Additionally, the "1% rule"[16] commonly followed in liquid rocket injector design may not be a sufficient constraint when designing an injector for unsteady operation.

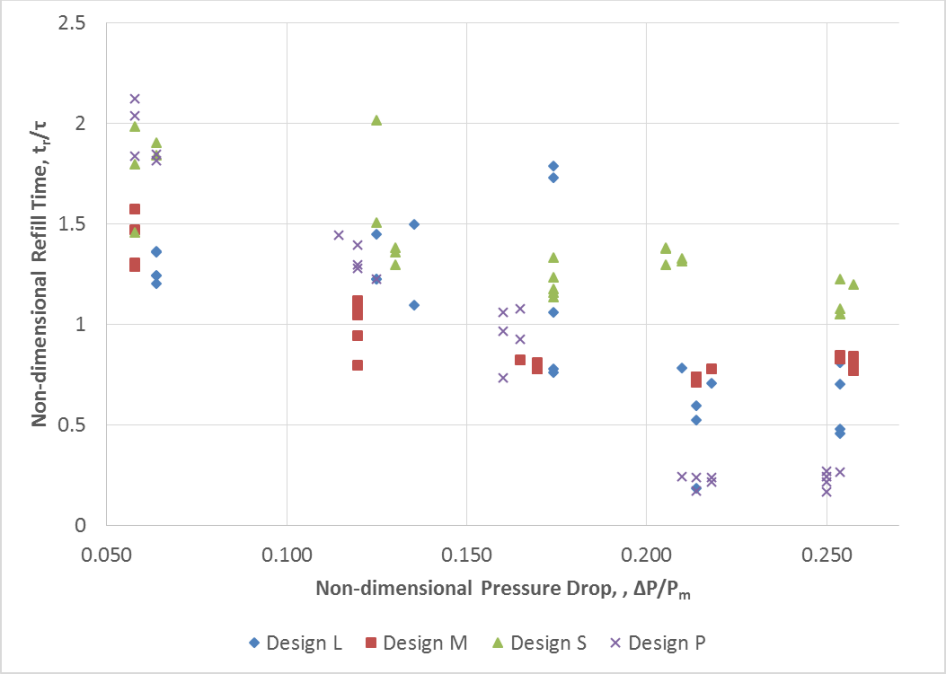

Figure 4-11. Plot of non-dimensional refill time vs. non-dimensional pressure drop across injector.

The recovery time of the injector is another, if not the most, important parameter in this study. In a PGC such as the RDE, the injector's recovery time factors in a crucial consideration relative to refilling of the reactants prior to arrival of the next detonation wave. Figure 4-11 presents plots of non-dimensional refill time vs. non-dimensional pressure drop. Design L, as before, shows significant scatter for the same reason. The remaining cases, however, display some interesting trends. Design S can be seen to have longer non-dimensional refill times than Design M. However, with the reduction in plenum area in Design P, we see a large reduction in refill time, even surpassing that of Design M at higher pressure drops. This implies that the plenum cross section is a parameter which can be used to change the stiffness of an injector to help achieve sustained detonation or augment the performance of the RDE.

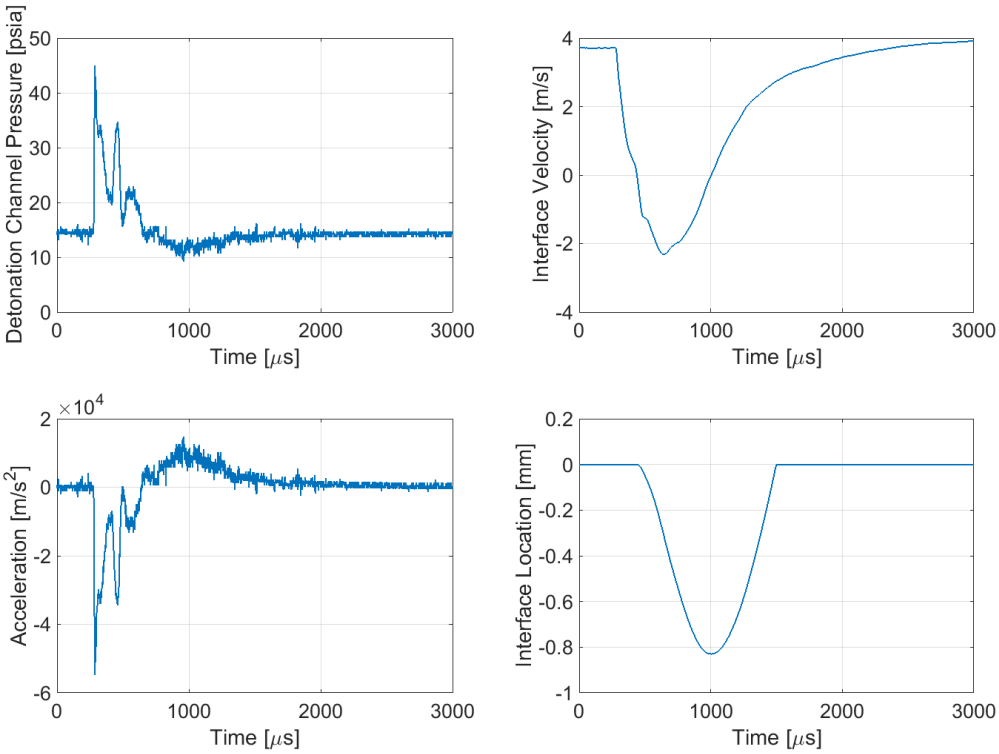

Figure 4-12. Sample output plots obtained from variable-mass model. Upper left: input pressure signal. Lower left: net acceleration on liquid column. Upper right: velocity of liquid-gas interface. Lower right: location of liquid-gas interface.

Figure 4-12 above is a sample output of the numerical model. The input pressure signal seen in the top left is from empirical data. It allows comparisons to be made between the model and the experiments. The pressure signal shown here is representative in amplitude, duration, and time integral of the other experiments for designs M, S, and P and for this reason shall be used to simplify computations of these cases. Judging from the peak pressure, a full Chapman-Jouguet detonation[17] had not been achieved. However, it is unimportant since the model is based on fundamental force balance calculations and should be able to take any form of pressure input to produce the predicted response. The bottom left plot shows the acceleration on the liquid in the injector orifice caused by the pressure pulse. As expected, it is a direct mirror of the pressure signal. The velocity profile in the top right shows how quickly the liquid-gas interface moves within the injector. Positive values indicate flow towards the detonation channel and negative values signify backflow. The last and most important plot is the time history of the liquid-gas interface location. From this plot the two parameters of interest are obtained: maximum backflow distance and recovery time. These are the two measurable quantities from the experiments and are therefore the bases of comparison. Computations were performed on all the test conditions so that the predictions could be compared with actual measurements.

Comparisons were made for designs L, M, and S. Design P was excluded since the model did not include provisions to consider plenum geometry and design P deviated significantly from a plain orifice. Let the non-dimensional error in backflow be defined as the difference between predicted and actual backflow distance divided by the injector length L and the non-dimensional error in refill be the difference between predicted and actual refill time divided by the orifice transit time τ. The results are plotted against non-dimensional injector pressure drop and Reynolds number in the following subsections. Points on the plots are separated into those which underwent complete or partial backflow during the experiment and those which showed limited backflow. The reason for plotting them separately is the difficulty in defining backflow distance and refill time during limited backflow as previously mentioned in the Methodology section. Being able to identify data points whose uncertainties are systematically larger could be helpful in

avoiding wrong conclusions. From the way the error values were defined, predictions are considered to be accurate if the points approach zero.

4.4 Error in Backflow Distance

On Figure 4-14, a clear upward-sloping trend may be observed in all three sets of data. Data points of design L show larger scatter due to the non-optimal flow path design, but the approach towards zero can be seen nonetheless. Design M shows a similar curve in its points. Design S' points, however, can be seen dipping in the region of $\Delta P/P_m \approx 0.2$ before climbing back up at $\Delta P/P_m \approx 0.25$. Since the method of measurement remained consistent throughout, it is unlikely that the occurrence was due to systematic error. It is possible that this cluster of data simply contained uncertainty biased towards lower values while the previous set was biased higher, leading to the appearance of a dip in the trend. The plot of the same error against Reynold number (Figure 4-15) reveals that the extent of turbulence in the liquid flow initially may heavily influence the way the liquid column responds to the pressure wave. While the model seemingly becomes more accurate at higher pressure drop or Reynolds number, most of those points are for limited backflow. At these pressure conditions, it was not possible to achieve partial backflow at the larger pressure differentials. The effect of turbulence on the applicability of the model would require a separate series of experiments carried out at higher initial chamber pressures to elucidate.

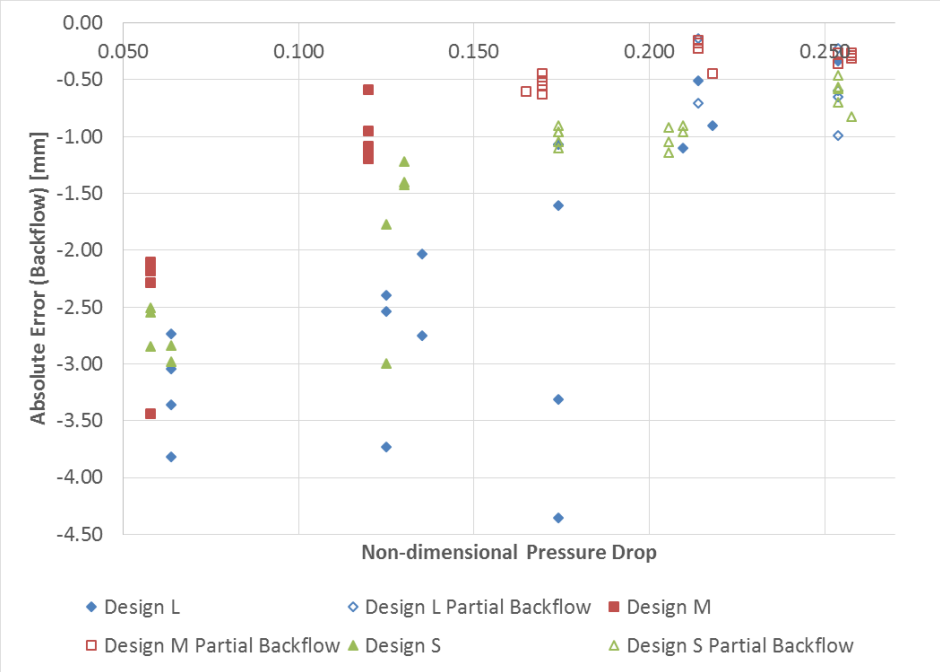

Figure 4-13. Plot of absolute error in backflow distance vs. non-dimensional pressure drop.

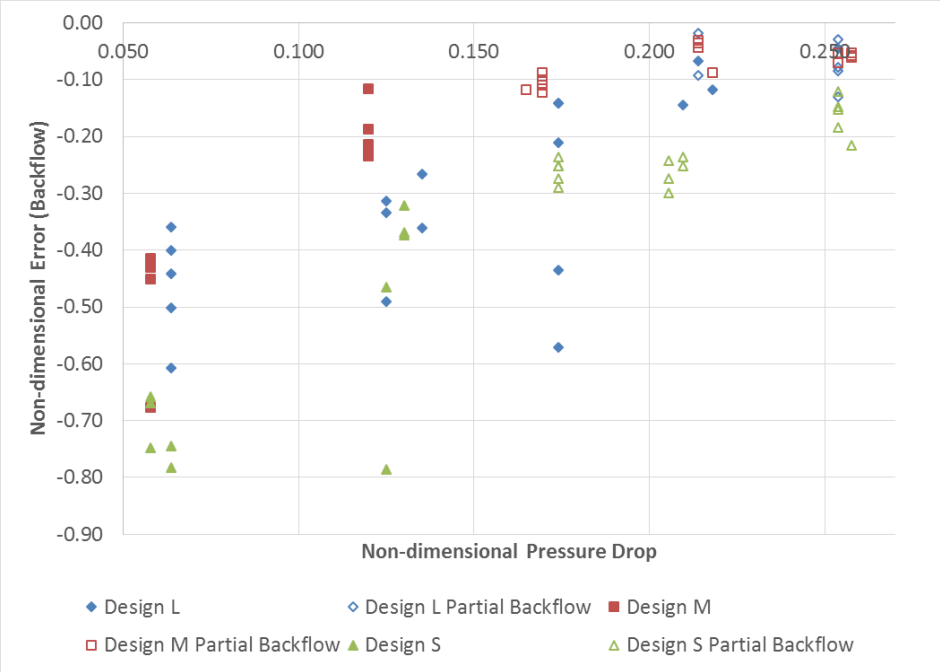

Figure 4-14. Plot of non-dimensional error in backflow distance vs. non-dimensional pressure drop.

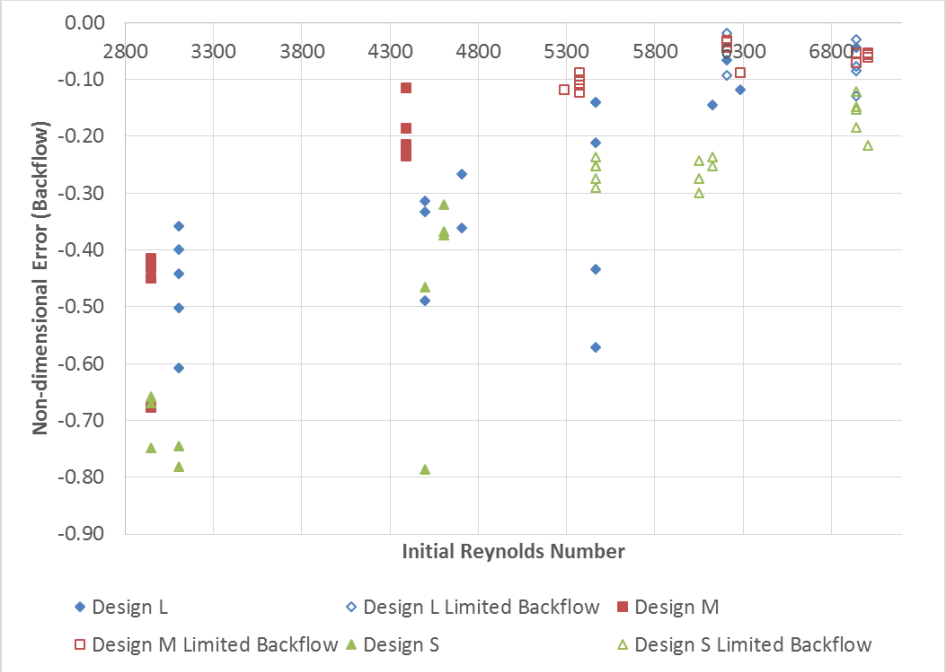

Figure 4-15. Plot of non-dimensional error in backflow distance vs. Reynolds number.

4.5 Error in Refill Time

In Figure 4-16, the plot shows a general upward sloping trend apart from the data points at the lowest pressure drop. It is a possibility that the flow regime at that pressure drop is significantly different from that at the rest of the manifold pressure settings such that the flow dynamics require a different model of prediction. The plots of non-dimensional error in refill time (Figure 4-17, Figure 4-18) appear mostly horizontal. Whether or not the horizontal trend would continue as Reynolds number continues increasing is unclear due to the very limited range of pressure drops investigated in this study.

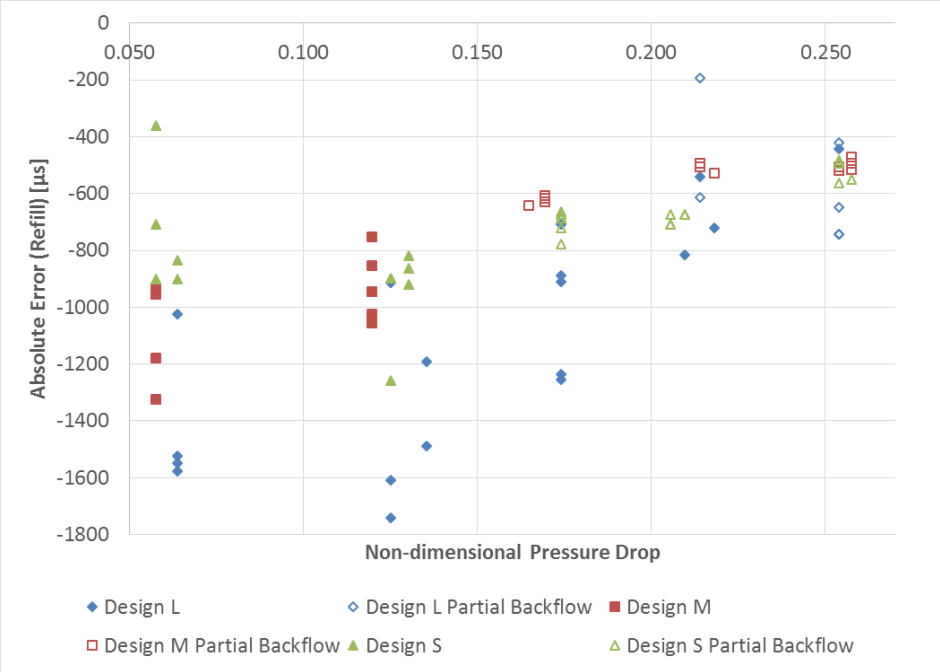

Figure 4-16. Plot of absolute error in refill time vs. non-dimensional pressure drop.

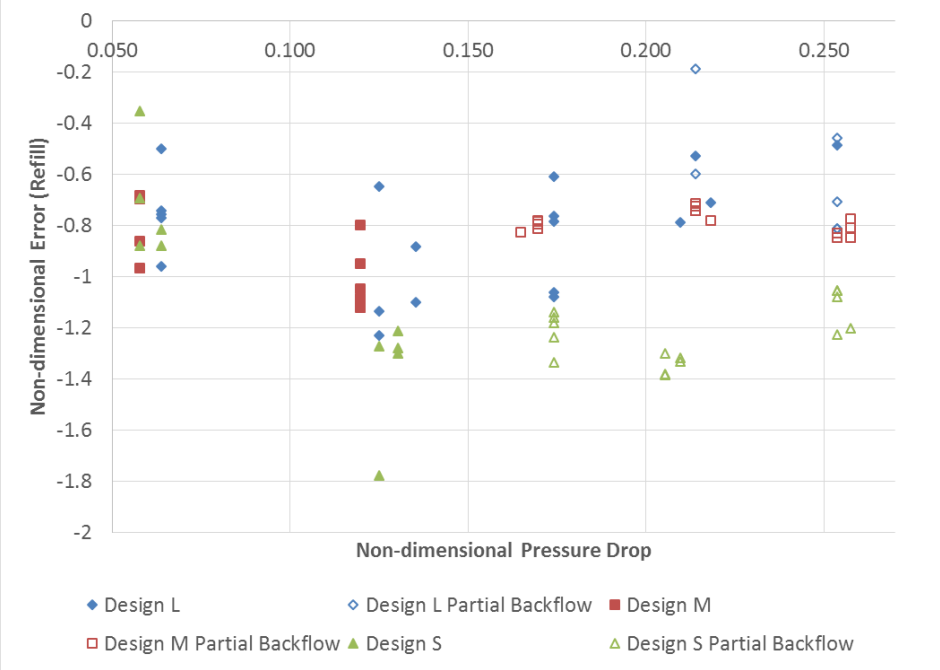

Figure 4-17. Plot of non-dimensional error in refill time vs. non-dimensional pressure drop.

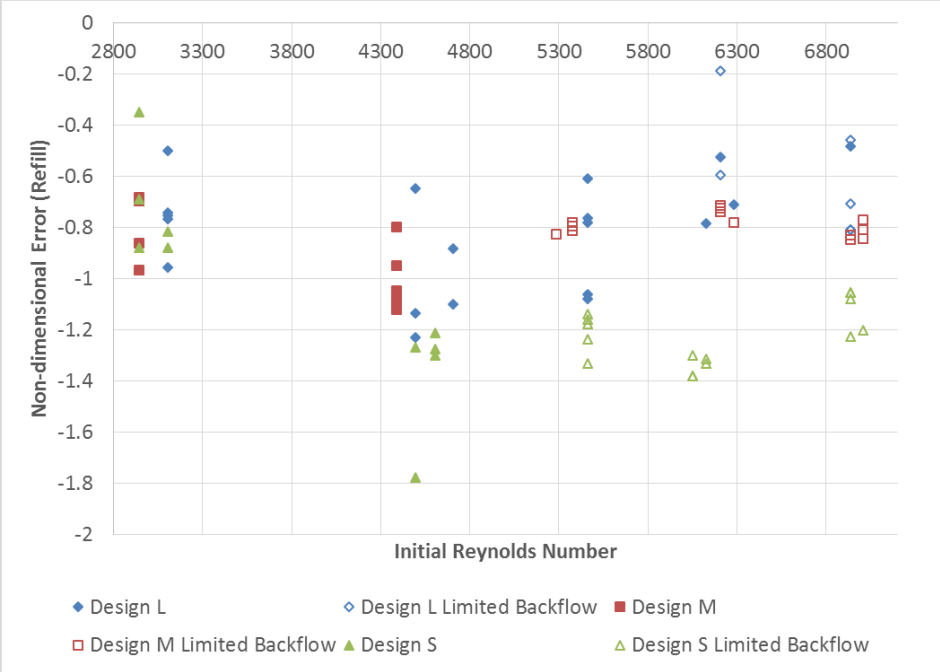

Figure 4-18. Plot of non-dimensional error in refill time vs. Reynolds number.

4.6 Potential Contributions to Error

Several possible sources of error have been considered, the first being the appropriateness of the 1-D assumption. Design S with its smallest L/D ratio of 4.5 is hardly one-dimensional, considering the relative size of its vena contracta to its length. Correspondingly, it displayed some of the largest errors in both backflow distance and refill time, seen in Figure 4-15 and Figure 4-18. Design L is expected to be the best represented by the 1-D model. However, aside from the error induced by the less consistent pressure measurements, it is also expected to have the thickest boundary layer and thus increased deviation from 1-D behavior. Another potential cause of error could also simply be the effect of thermal drift on the representative pressure trace used.

The large error seen in the refill time computations require special address because of the importance of being able to predict this parameter accurately. The first venue of investigation is in the boundary layer development of the designed injectors. 2-D

axisymmetric CFD simulations of the injectors were performed over three different injector ΔP – 2psi, 4psi, and 5psi – to provide estimates of initial boundary layer thickness during the experiments. The goal is to produce plots of error as a function of boundary layer thickness. Boundary layer thickness was chosen as the distance from the wall where axial flow velocity reaches 99% of the centerline velocity. Results reveal that under the flow conditions bracketed by the experiments, the boundary layer was still developing at the exit of the longest orifice. The steeper fall in axial velocity near the channel wall could imply greater sensitivity to backpressure and lower predictability in the flow dynamics. A plot of the axial velocity profile vs. radius of orifice is shown in Figure 4-19 shows a large plateau in velocity extending from the centerline instead of a parabolic profile characteristic of fully developed flow.

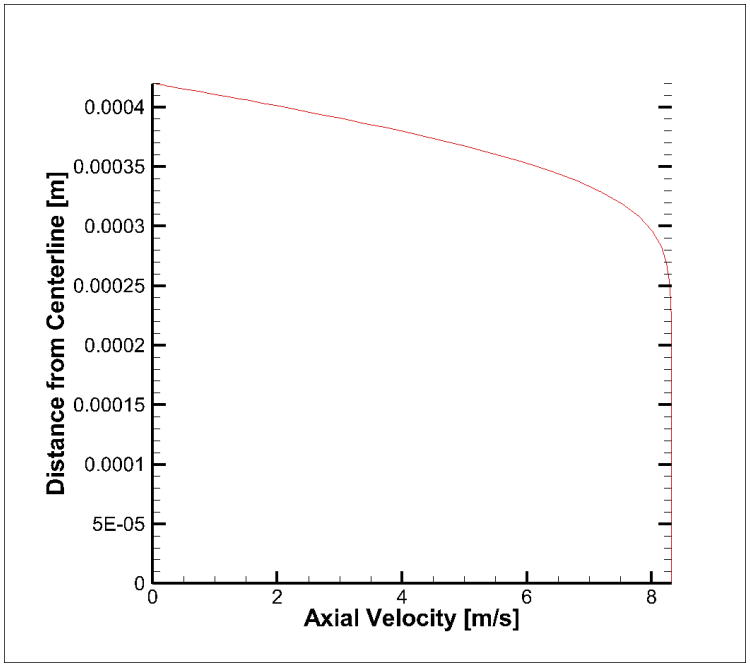

Figure 4-19. Axial velocity profile at exit of injector design L at ΔP = 5psi.

Curve fits were applied to the results of the CFD analysis to yield equations (shown in Figure 4-20) which were used to estimate boundary layer thickness for each of the experiments. The power curve was chosen on the assumption that boundary layer development in a circular channel would follow a similar trend to that over a flat plate,

whose empirical relations are power functions of Reynolds number. Non-dimensional errors of backflow distance and refill time were then plotted against non-dimensional boundary layer thickness, shown in Figure 4-21 and Figure 4-22.

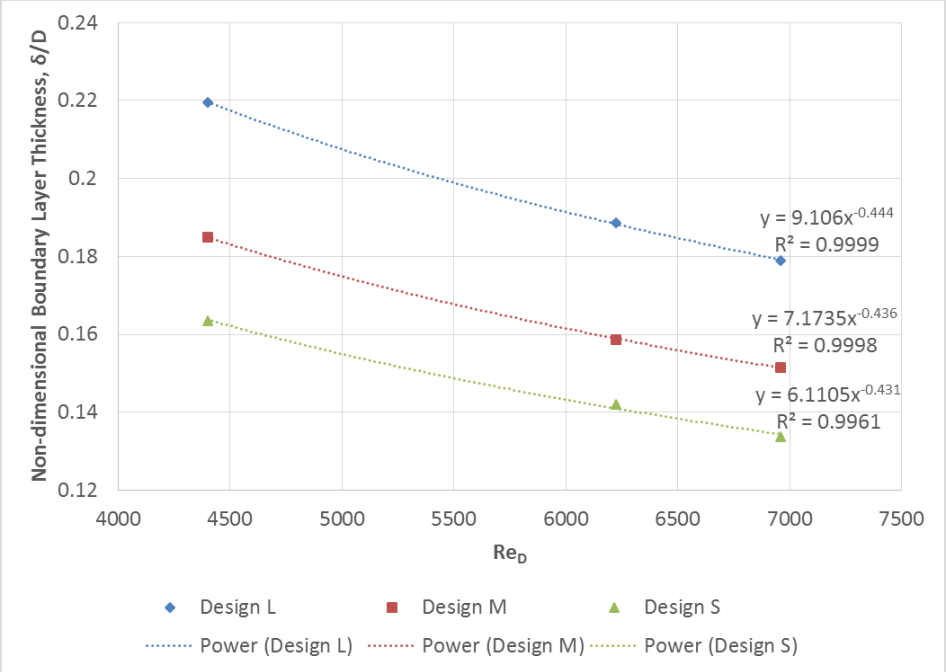

Figure 4-20. Plot of non-dimensional boundary layer thickness vs. Reynolds number showing power curve fits.

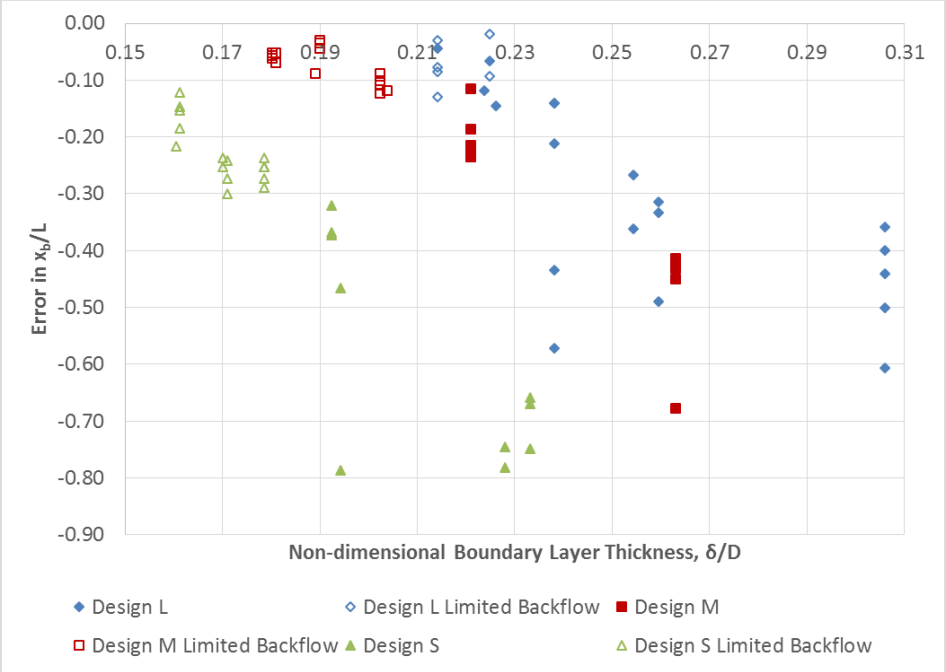

Figure 4-21. Plot of non-dimensional error in backflow distance vs. non-dimensional boundary layer thickness.

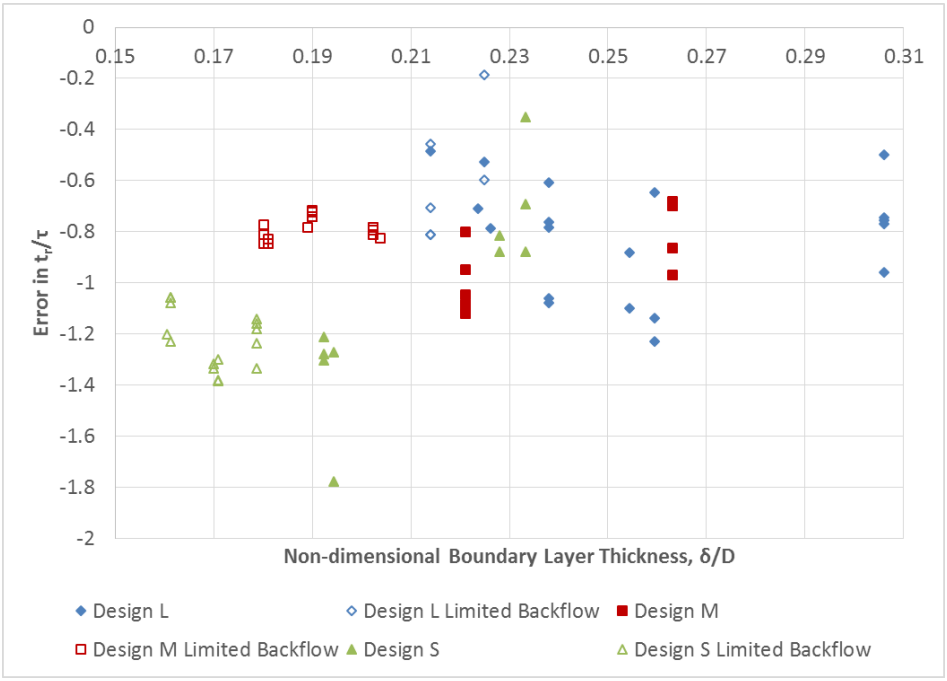

Figure 4-22. Plot of non-dimensional error in refill time vs. non-dimensional boundary layer thickness.

In Figure 4-21, it is readily apparent that for each set of data, the error increased as the boundary layer became thicker. It implies that in high speed flows, such as in rocket applications, the 1-D model may be suitable for the purpose of evaluating injector length. On the other hand, the lack of any trend in Figure 4-22 seems to suggest that there is no strong correlation between the accuracy of refill time prediction and boundary layer thickness.

The other possible source of error could be the discharge coefficient of the injectors. The catch and weigh method was employed to measure the discharge coefficient C_d of the injectors. Typically, C_d increases with flow rate until cavitation occurs in the orifice, after which it plateaus to a stable value. For the catch and weigh, upstream pressures were 10, 15, and 20 psig. For these pressure drops, the C_d values were found to be in the sloping region. In the dynamic response experiments, the maximum pressure drop was 5psi. This means that C_d was not constant when downstream pressure fluctuated with the passage of the wave and could very likely introduce more uncertainty to the experiment. A chart of the C_d of each injector at various tested pressures is shown in Figure 4-23.

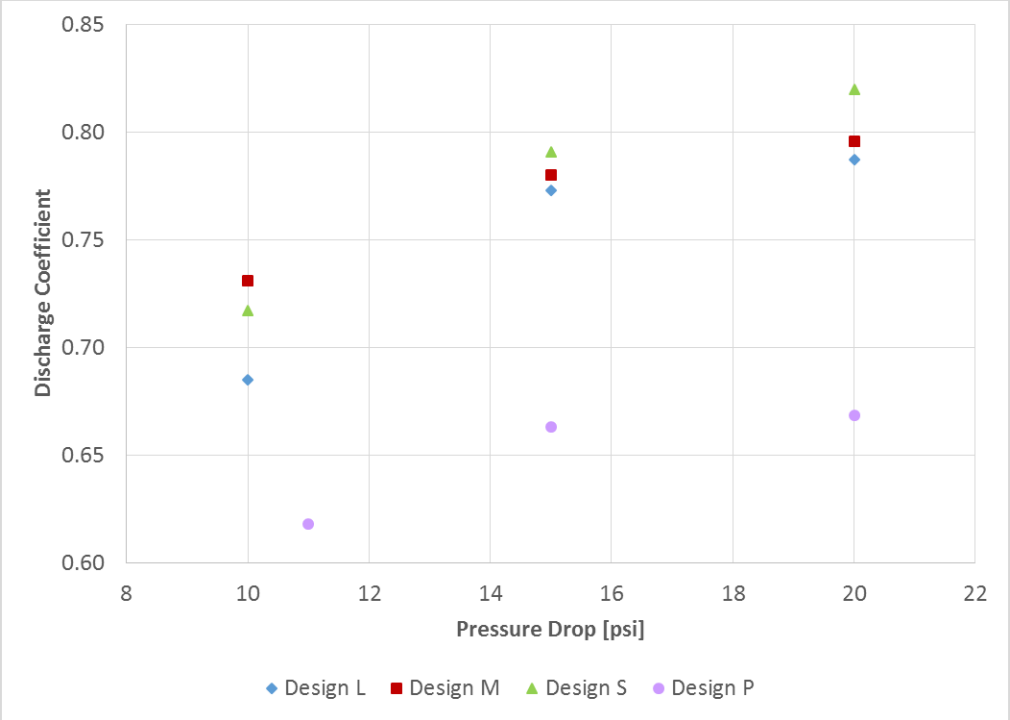

Figure 4-23. Discharge coefficient vs. pressure drop of tested injectors

CHAPTER 5. CONCLUSIONS AND RECOMMENDATIONS

5.1 Conclusions

A series of experiments has been conducted to investigate the transient response of a liquid injector when subjected to a steep-fronted transverse pressure wave. The experimental platform exposed a single plain-orifice atomizer to a weak hydrogen/oxygen detonation in a transparent structure. Water was the injected fluid and injection pressures of 1-5 psig were used in injectors that varied in length from 0.15-0.30in (3.81-7.62 mm). A companion high-frequency pressure measurement provided simultaneous pressure and surface shapes during fluid backflow within the injector. A one-dimensional flow model was also created to assess abilities to predict the measured response on this basis. A total of 100 experiments were conducted at ambient pressure conditions.

Since the experiments were performed at ambient pressure, they are far from representative of rocket systems. However, they do provide a glimpse into the subject which is of importance to injector dynamic response in pressure gain combustion devices. The experiments have shown that the behavior of the liquid is far from one-dimensional; instead, the mechanism for backflow is complex because of the boundary layer dynamics which most likely play a major role in gas penetration, especially at low injector Reynolds numbers. Specifically, the detonation wave first propagates into the injector along the boundary layer on the upwind-side of the orifice. It remains unclear how varying the injector length affects backflow distance or refill time due to the lack of consistent order in the results. However, it was revealed in the experiments with the injector with the narrower plenum (Design P) that the cross sectional area of the

injector's plenum significantly influences its dynamic response; a narrower plenum results in reduction of both backflow distance and refill time for injectors of the same length. This implies that adjustments to the plenum design could potentially be used to augment an injector's performance.

The 1-D model shows promise in the prediction of backflow distance at higher initial Reynolds numbers, but lacks accuracy in predicting refill time, whose prediction error did not appear to be dependent on Reynolds number nor boundary layer thickness. However, it (error in refill time) does appear to have a horizontal distribution over the range of pressure differentials tested. It is important to note that a large portion of the data presented reside in cases where the injector underwent limited backflow which the 1-D model was incapable of capturing and as such, the comparison carried greater uncertainty. Performing the experiments at ambient pressure presented a serious limitation to the range of injector response that could be obtained because of the low pressure wave strength, i.e. the injectors tend to reach the point of limited backflow at low pressure drop ($\Delta P = \sim 3psi$). Additionally, the discharge coefficients of the injectors at these test conditions were still dependent on the pressure differential which meant that at each pressure differential setting, the injectors were characteristically different. Due to the highly dynamic mode of operation, the fluctuating discharge coefficient was likely to have exacerbated the deviation of injector response from the ideal scenario.

On the whole, the 1-D model may be a viable tool for evaluating the length of an injector, i.e. whether an injector of length L is sufficiently long such as to prevent complete backflow when a pressure signal is applied, but not its recovery time. If further experiments are able to show that the non-dimensional error in refill time continues in a horizontal trend at yet higher Reynolds numbers, it may be possible to simply apply a scaling factor to the predictions given by the model.

5.2 Recommendations for Future Work

Moving forward, similar injector studies should be performed at elevated pressures more representative of PGC devices (>10atm). Since the pressure gain across a

detonation wave is proportional to the initial pressure, the amplitude of the pressure wave will be much greater than what was seen in this study. It will allow a significantly larger range of injector pressure differentials to be tested and compared with the 1-D model. The greater pressure drop across the injector will likely result in a more developed turbulent flow, making boundary layer effects less prominent. At higher flow speeds, the injectors will also be expected to hold stable discharge coefficients over the range of conditions tested. This will lead to a more consistent comparison of data. Lastly, the increased range of tested Reynolds numbers will provide insight to whether injector response is more strongly influenced by the absolute or fraction of pressure drop across the injector. Possessing this piece of information would allow the establishment of an envelope for which the model can be expected to work at a greater confidence level.

In the current study, the injectors are oriented perpendicularly to the exit plane. Further investigation could be done on injectors tilted at an angle – both upwind and downwind – to uncover the advantages and disadvantages of each orientation. On top of that, the response of multiple injector elements sharing a common plenum should also be studied since it would be the case in an actual injector. Finally, it may also be worthwhile to design the test article to allow side relief, as is the case with a RDE.

The test article will require significant modifications to withstand the pressure levels associated with the abovementioned recommendation. Material strength constraints will most likely point towards a setup which is predominantly made of stainless steel with a small, optically-accessible insert containing the injector element. The flow paths will need to be designed as an enclosed volume to allow pre-pressurization. A catchment tank will also be needed downstream of the detonation channel exit such that the mean pressure of the system would not increase by a significant amount following the detonation event. It is also recommended that silicon-based pressure transducers be avoided for their thermal sensitivity.

LIST OF REFERENCES

LIST OF REFERENCES

[1]Daniau, E., Falempin, F., & Zhdan, S., "Pulsed and Rotating Detonation Propulsion Systems : First Step Toward Operational Engines," *AIAA/CIRA 13th International Space Planes and Hypersonics Systems and Technologies* [online database], 2005. [cited June 2015]

[2]Nordeen, C. A. et al., "Thermodynamic Modeling of a Rotating Detonation Engine," *49th AIAA Aerospace Sciences Meeting* [online database], 2011. [cited June 2015]

[3]Shimo, M. and Heister, S. D., "Schlieren Visualization of Multicyclic Flame Acceleration Process in Valveless Pulsed Detonation Combustors", Combustion Science and Technology, 180: 1613–1636, 2008.

[4]Lu, F., Braun, E., "Rotating Detonation Wave Propulsion: Experimental Challenges, Modeling, and Engine Concepts," *Journal of Propulsion and Power, 2014,* Vol. 30, No. 5, pp. 1125-1142.

[5]Bykovskii, F. A., Zhdan, S. A., & Vedernikov, E. F., "Continuous Spin Detonations," *Journal of Propulsion and Power,* 2006, Vol. 22, No. 6, pp. 1204-1216.

[6]MacDonald, M., "On the Nonlinear Dynamic Response of Plain Orifice Atomizers/Injectors," M.S. Thesis, School of Aeronautics and Astronautics, Purdue University, West Lafayette, IN, 2006.

[7]Harrje, D., Reardon, F., "Liquid Propellant Rocket Combustion Instability," NASA SP-194, 1972, pp. 373-377.

[8]Reba, I., Brosilow, C., "Combustion Instability: Liquid Stream and Droplet Behavior. Part III: The Response of Liquid Jets to Large Amplitude Sonic Oscillations," WADC TR 59-720, Wright Air Development Center, United States Air Force, 1960.

[9]Felderhof, B. U., "Transient Flow of a Viscous Incompressible Fluid in a Circular Tube After a Sudden Point Impulse," *Journal of Fluid Mechanics*, Vol. 637, Cambridge University Press, 2009, pp. 285-303.

[10]Braun, E. et al., "Experimental Study of a High-Frequency Fluidic Valve Fuel Injector," *47th AIAA Joint Propulsion Conference* [online database], 2011. [cited June 2015]

[11]Naples, A., Hoke, J., and Schauer, F., "Experimental Investigation of a Rotating Detonation Engine Fuel Injector Temporal Response," *53rd AIAA Aerospace Sciences Meeting* [online database], 2015. [cited June 2015]

[12]Wylie, E. B. and Streeter, V., *Fluid Transients in Systems*, 1st ed., Prentice Hall, New Jersey, 1993.

[13]Kindracki, J., Wolanski, P., and Gut, Z., "Experimental Research on the Rotating Detonation in Gaseous Fuels-Oxygen Mixtures," *Shock Waves*, Vol. 21, 2011, pp. 75-84.

[14]Peng, L. et al., "Ignition Experiment with Automotive Spark on Rotating Detonation Engine," *International Journal of Hydrogen Energy*, Vol. 40, 2015, pp. 8465-8474.

[15]Colebrook, C. F., & White, C. M., "Experiments with Fluid Friction in Roughened Pipes," *Proceedings of the Royal Society of London. Series A, Mathematical and Physical Sciences*, 1937, Vol. 161, No. 906, pp. 367-381.

[16]Huzel, D., Huang, D., *Modern Engineering for Design of Liquid-Propellant Rocket Engines*, AIAA, 1992, pp. 107.

[17]NASA Chemical Equilibrium with Applications, Software, NASA Glenn Research Center, Cleveland, OH, 2005.

[18]Lim, D. et al., "Transient Response of a Liquid Injector to a Transverse Pressure Wave," *51st AIAA/SAE/ASEE Joint Propulsion Conference* [online database], 2015.

APPENDICES

Appendix A Hardware Design and Technical Specifications

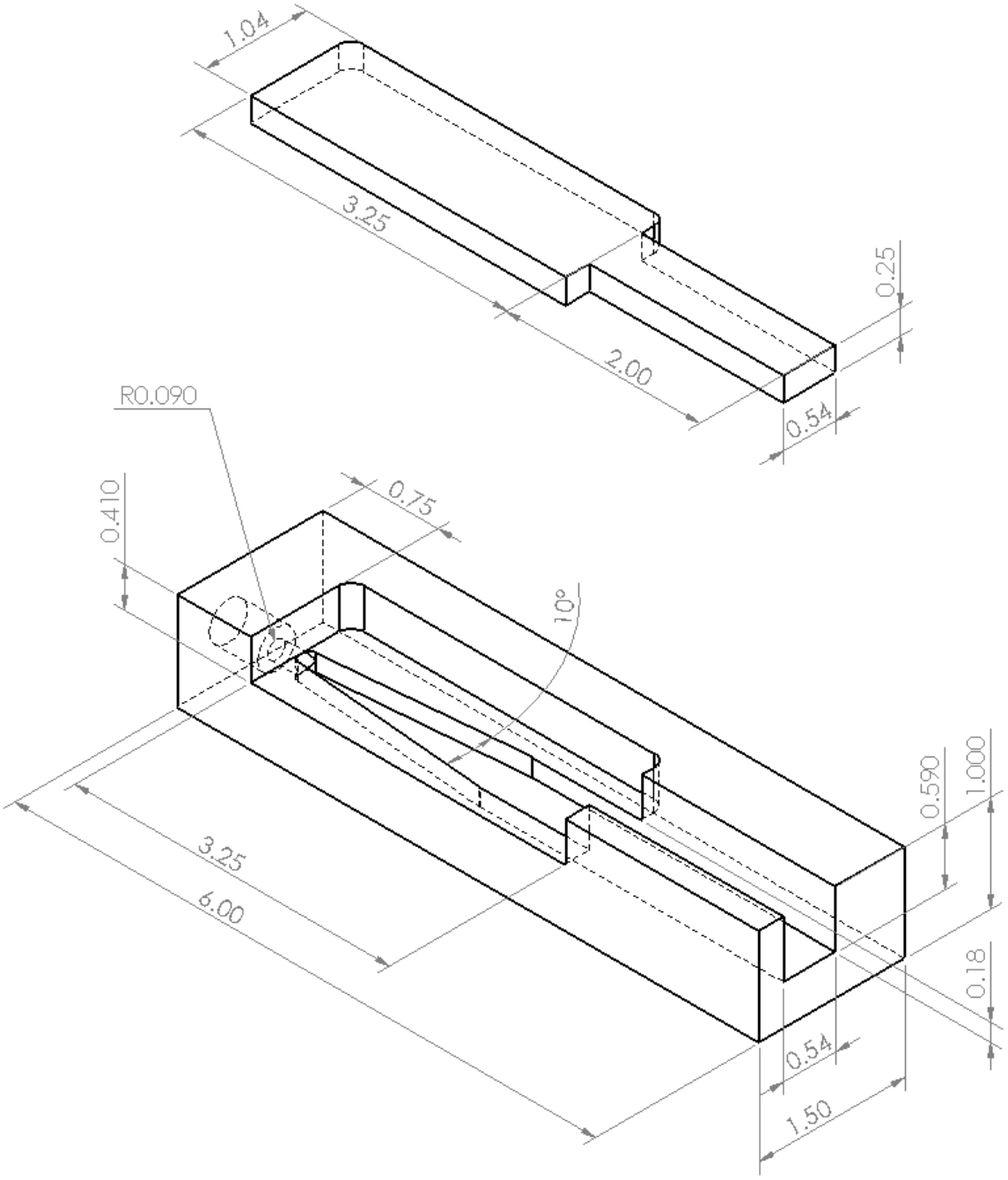

Figure A-1. Drawing of transition channel section showing major dimensions in inches.

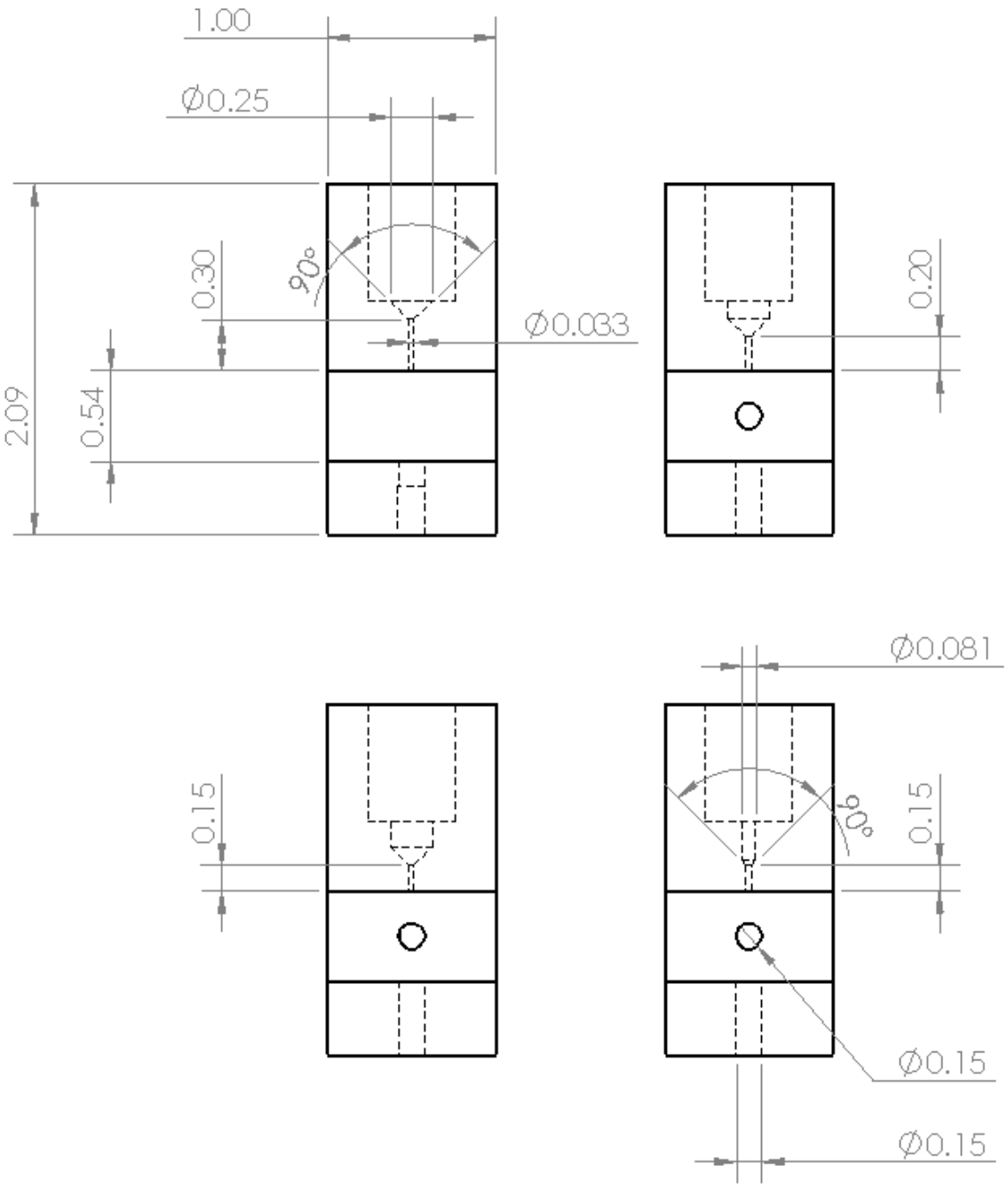

Figure A-2. Drawings of injector modules showing major dimensions in inches. All injector orifices have a diameter of 0.033in (0.84mm).

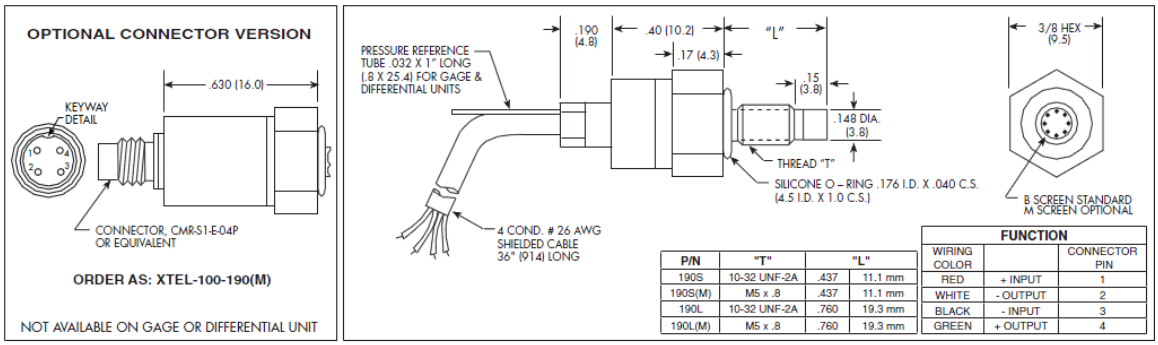

P/N	"T"		"L"
190S	10-32 UNF-2A	.437	11.1 mm
190S(M)	M5 x .8	.437	11.1 mm
190L	10-32 UNF-2A	.760	19.3 mm
190L(M)	M5 x .8	.760	19.3 mm

FUNCTION		
WIRING COLOR		CONNECTOR PIN
RED	+ INPUT	1
WHITE	- OUTPUT	2
BLACK	- INPUT	3
GREEN	+ OUTPUT	4

INPUT	Pressure Range	0.7 10	1.0 15	1.7 25	3.5 50	7 100	17 250	35 500	70 1000	140 BAR 2000 PSI
	Operational Mode	Absolute, Gage, Differential		Absolute, Gage, Sealed Gage, Differential			Absolute, Sealed Gage			
	Over Pressure	2 Times Rated Pressure to a Maximum of 3000 PSI (210 BAR)								
	Burst Pressure	3 Times Rated Pressure to a Maximum of 5000 PSI (350 BAR)								
	Pressure Media	Most Conductive Liquids and Gases - Please Consult Factory (All Media May Not Be Suitable With O-Ring Supplied)								
	Rated Electrical Excitation	10 VDC								
	Maximum Electrical Excitation	12 VDC								
	Input Impedance	1000 Ohms (Min.)								
OUTPUT	Output Impedance	1000 Ohms (Nom.)								
	Full Scale Output (FSO)	100 mV (Nom.)								
	Residual Unbalance	± 5 mV (Typ.)								
	Combined Non-Linearity, Hysteresis and Repeatability	± 0.1% FSO BFSL (Typ.), ± 0.5% FSO (Max.)								
	Resolution	Infinitesimal								
	Natural Frequency of Sensor Without Screen (KHz) (Typ.)	175	200	240	300	380	550	700	1000	1400
	Acceleration Sensitivity % FS/g Perpendicular	$1.0x10^{-3}$	$6.5x10^{-4}$	$5.0x10^{-4}$	$3.0x10^{-4}$	$1.5x10^{-4}$	$1.0x10^{-4}$	$6.0x10^{-5}$	$4.5x10^{-5}$	$2.0x10^{-5}$
	Insulation Resistance	100 Megohm Min. @ 50 VDC								
ENVIRONMENTAL	Operating Temperature Range	-65°F to +525°F (-55°C to +273°C)								
	Compensated Temperature Range	+80°F to +450°F (+25°C to +232°C)								
	Thermal Zero Shift	± 1% FS/100°F (Typ.)								
	Thermal Sensitivity Shift	± 1% /100°F (Typ.)								
	Steady Acceleration	10,000g. (Max.)								
	Linear Vibration	10-2,000 Hz Sine, 100g. (Max.)								
PHYSICAL	Electrical Connection	4 Conductor 26 AWG Shielded Cable 36" Long								
	Weight	4 Grams (Nom.) Excluding Cable								
	Pressure Sensing Principle	Fully Active Four Arm Wheatstone Bridge Dielectrically Isolated Silicon on Silicon Patented Leadless Technology								
	Mounting Torque	15 Inch-Pounds (Max.) 1.7 Nm								

Figure A-3. Technical specifications of Kulite™ XTEL-190 high frequency pressure transducer used in pressure wave measurement. Extracted from http://www.kulite.com.

Appendix B Additional Results and Figures

Table B-1. Integrated pressure wave impulse size corresponding to each test run for Design L.

Test Date		
5/9/2015		
Injector Length [in (mm)]	**Plenum Diameter [in (mm)]**	
0.30 (7.62)	0.25 (6.35)	
Test No.	**Manifold Pressure [psia]**	**Wave Impulse [psi-s]**
1	15.7	0.0061
2	15.7	0.0061
3	15.7	0.0060
4	15.7	0.0069
5	15.7	0.0049
6	16.8	0.0056
7	16.8	0.0079
8	16.8	0.0063
9	17.0	0.0048
10	17.0	0.0075
11	17.8	0.0045
12	17.8	0.0064
13	17.8	0.0093
14	17.8	0.0069
15	17.8	0.0099
16	18.6	0.0071
17	18.7	0.0066
18	18.7	0.0077
19	18.7	0.0051
20	18.8	0.0078
21	19.7	0.0065
22	19.7	0.0068
23	19.7	0.0070
24	19.7	0.0075
25	19.7	0.0068

Table B-2. Integrated pressure wave impulse size corresponding to each test run for Design M.

Test Date		
5/16/2015		
Injector Length [in (mm)]	**Plenum Diameter [in (mm)]**	
0.20 (5.08)	0.25 (6.35)	
Test No.	**Manifold Pressure [psia]**	**Wave Impulse [psi-s]**
1	15.6	0.0042*
2	15.6	0.0043*
3	15.6	0.0047*
4	15.6	0.0205*
5	15.6	0.0045*
6	16.7	0.0042*
7	16.7	0.0050
8	16.7	0.0050
9	16.7	0.0044*
10	16.7	0.0050
11	17.7	0.0042*
12	17.7	0.0042*
13	17.7	0.0044*
14	17.6	0.0042
15	17.7	0.0043*
16	18.7	0.0044*
17	18.7	0.0045
18	18.7	0.0046*
19	18.7	0.0051
20	18.8	0.0053
21	19.8	0.0037*
22	19.7	0.0036*
23	19.7	0.0033*
24	19.8	0.0030*
25	19.8	0.0034*

* - Pressure signal contaminated by thermal drift.

Table B-3. Integrated pressure wave impulse size corresponding to each test run for Design S.

Test Date		
5/23/2015		
Injector Length [in (mm)]	**Plenum Diameter [in (mm)]**	
0.15 (3.81)	0.25 (6.35)	
Test No.	**Manifold Pressure [psia]**	**Wave Impulse [psi-s]**
1	15.6	0.006*
4	15.6	0.0047*
5	15.7	0.0043*
6	15.6	0.0048*
7	15.7	0.0049
9	16.8	0.005*
10	16.8	0.0045*
11	16.9	0.0045*
12	16.9	0.0043*
14	16.9	0.0043*
15	17.8	0.0047*
16	17.8	0.0047
17	17.8	0.0042*
18	17.8	0.0047
19	17.8	0.0045
21	18.5	0.0052*
22	18.5	0.0045*
23	18.6	0.0049*
24	18.5	0.0045*
25	18.6	0.0046*
26	19.8	0.0045*
27	19.7	0.0046*
28	19.7	0.0049
29	19.7	0.0042*
30	19.7	0.0042*

* - Pressure signal contaminated by thermal drift.

Table B-4. Integrated pressure wave impulse size corresponding to each test run for Design P.

Test Date		
5/30/2015		
Injector Length [in (mm)]	**Plenum Diameter [in (mm)]**	
0.15 (3.81)	0.081 (2.06)	
Test No.	**Manifold Pressure [psia]**	**Wave Impulse [psi-s]**
3	15.7	0.0045
4	15.7	0.0038*
5	15.6	0.0036*
6	15.6	0.0041*
7	15.6	0.0041*
9	16.8	0.0048
10	16.7	0.0041
14	16.7	0.0037*
15	16.7	0.0041
16	16.6	0.0037*
17	17.6	0.0037*
18	17.6	0.0041
19	17.5	0.0039*
20	17.5	0.0044
21	17.5	0.0042
22	18.7	0.0038*
23	18.7	0.0038*
24	18.8	0.0041*
25	18.8	0.0047
26	18.6	0.0049
27	19.7	0.0040*
28	19.6	0.0052
29	19.6	0.0440
30	19.6	0.0040*
31	19.6	0.0046

* - Pressure signal contaminated by thermal drift.

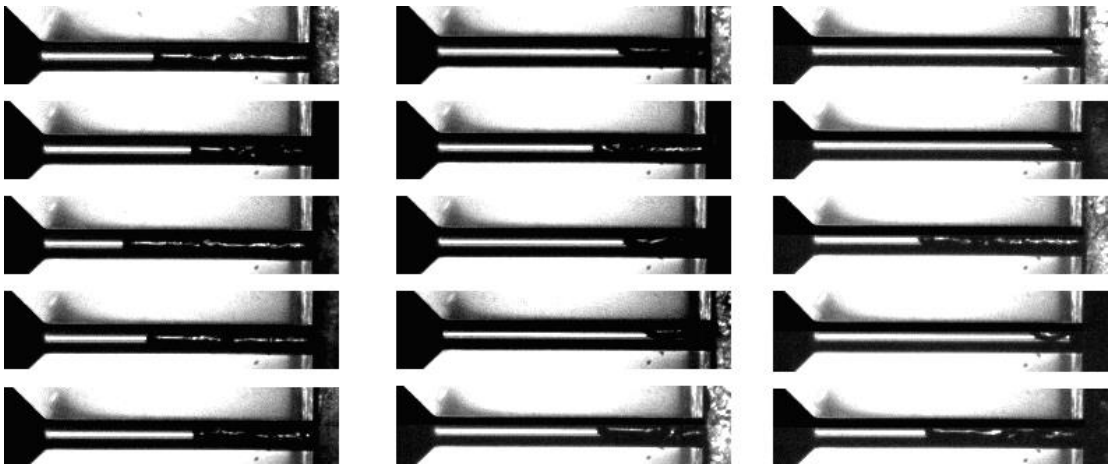

(a) **(b)** **(c)**

Figure B-1. Snapshots of instances at which maximum backflow is attained for each test using 0.30in injector. Manifold pressure in (a): 15.7psia, (b): 16.8psia, (c): 17.8psia.

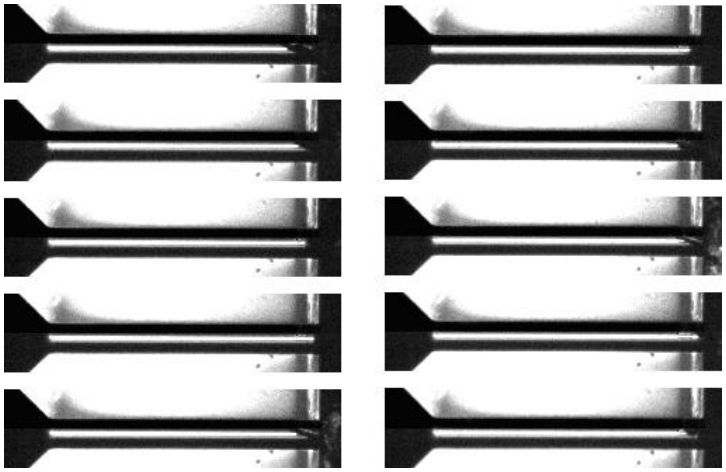

(d) **(e)**

Figure B-2. Snapshots of instances at which maximum backflow is attained for each test using 0.30in injector. Manifold pressure in (d): 18.7psia, (e): 19.7psia.

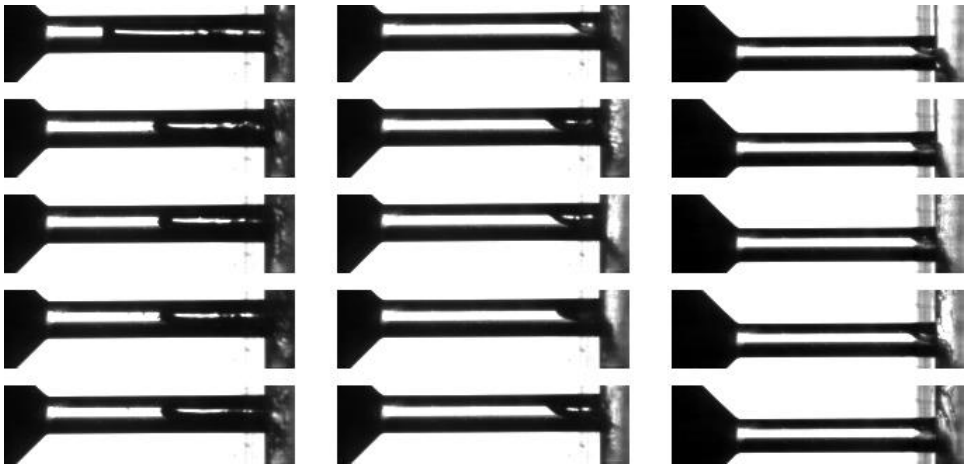

(a) **(b)** **(c)**

Figure B-3. Snapshots of instances at which maximum backflow is attained for each test using 0.20in injector. Manifold pressure in (a): 15.6psia, (b): 16.7psia, (c): 17.7psia. Higher manifold pressures not shown due to similarity of backflow extent as (c).

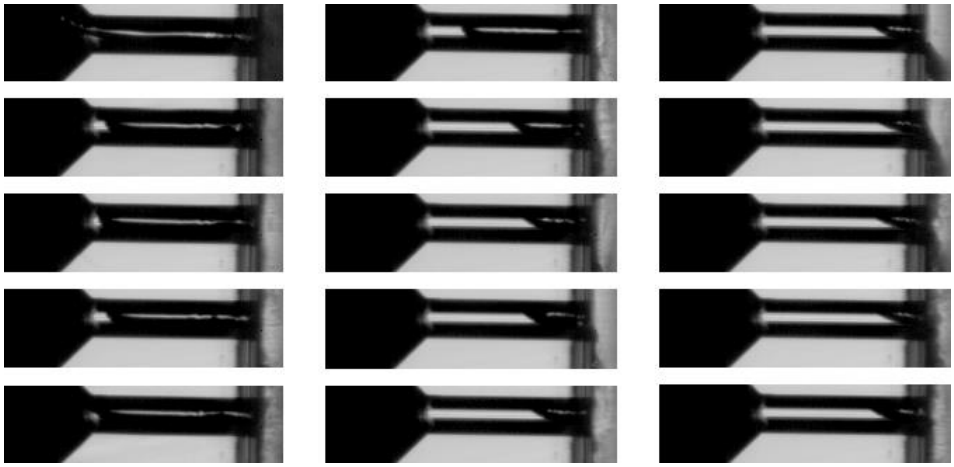

(a) **(b)** **(c)**

Figure B-4. Snapshots of instances at which maximum backflow is attained for each test using 0.15in injector. Manifold pressure in (a): 15.6psia, (b): 16.9psia, (c): 17.8psia.

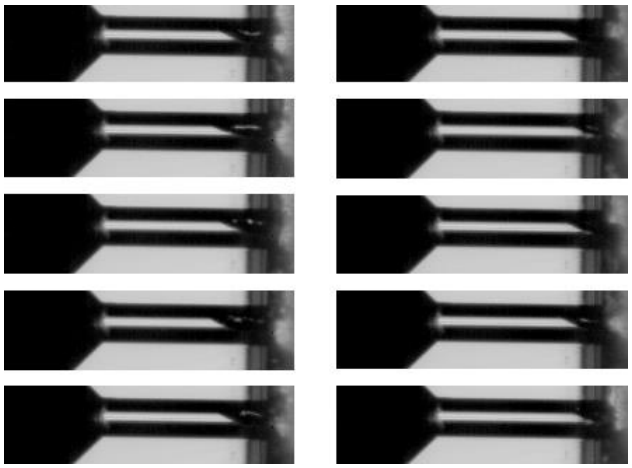

(d) **(e)**

Figure B-5. Snapshots of instances at which maximum backflow is attained for each test using 0.15in injector. Manifold pressure in (d): 18.5psia, (e): 19.7psia.

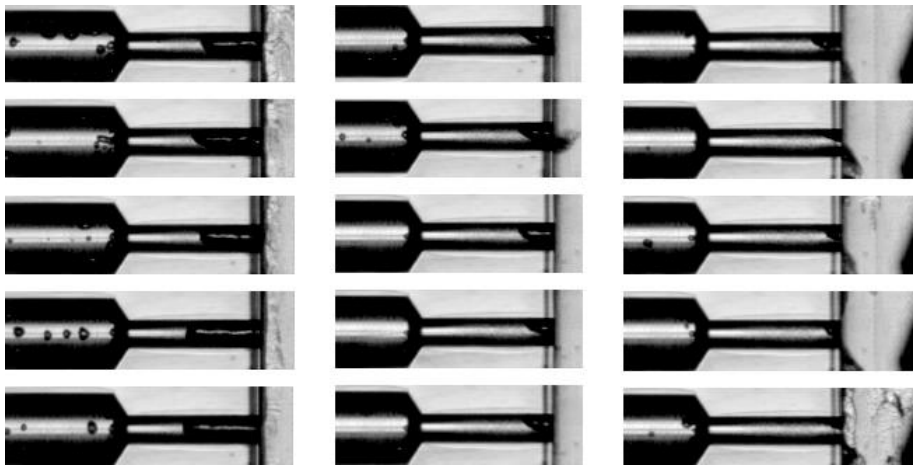

(a) **(b)** **(c)**

Figure B-6. Snapshots of instances at which maximum backflow is attained for each test using 0.15in injector with reduced plenum. Manifold pressure in (a): 15.6psia, (b): 16.7psia, (c): 17.5psia. Higher manifold pressures not shown due to similarity of backflow extent as (c).